ANALYSIS OF ENTRAINMENT AND CLAMPING LOSS IN AN OPTICALLY ACTUATED MEMS

A Dissertation

Presented to the Faculty of the Graduate School

of Cornell University

in Partial Fulfillment of the Requirements for the Degree of

Doctor of Philosophy

by

Manoj Pandey

January 2008

ANALYSIS OF ENTRAINMENT AND CLAMPING LOSS IN AN OPTICALLY ACTUATED MEMS

Manoj Pandey, Ph.D.

Cornell University 2008

This thesis presents a study of thin, planar, radio frequency MEMS resonators that are shown to self-oscillate in the absence of external forcing, when illuminated by a DC laser of sufficient amplitude. Entrainment or frequency locking is achieved in these devices when an external forcing strong enough and close in frequency to that of the unforced oscillations is applied. The forcing can be accomplished either parametrically, by modulating the laser beam incident on the oscillator, or nonparametrically, using inertial driving. The system exhibits both 2:1 and 1:1 resonances, as well as quasiperiodic motions and hysteresis. Dynamics of a three dimensional system of coupled thermo-mechanical model for the forced disc resonator is studied, using a perturbation scheme. Perturbation results show that the model agrees well with experiments and explain how and where transitions into and out of entrainment occur. Simpler canonical models showing similar behavior are also studied.

Next a method to improve Quality factor (Q) of these devices is studied. Q is a measure of damping and models the total losses in a dynamical system. As MEMS vibrates, a fraction of its vibration energy is transmitted to the substrate upon which the MEMS are fabricated. A large component of this energy is carried away as surface acoustic waves (SAW). This energy is either scattered or dissipated into the relatively infinite expanse of the substrate and termed as anchor loss in the system. A design that improves the Q of dome shaped oscillators by up to 4 by

reflecting surface wave energy back to the MEMS is demonstrated. Wave reflection occurs at trenches fabricated in a circle around the MEMS. The trench creates a "mesa" that provides partial mechanical isolation to the MEMS. Finite element analysis (FEA) is used to model these losses with infinite elements acting as quiet boundary for the truncated substrate domain. These boundaries absorb most of the outgoing energy and model the relatively infinite expanse of the substrate. The results predicted by the model agree well with the experiments and are also able to predict the experimentally observed improvement due to the presence of a mesa.

BIOGRAPHICAL SKETCH

Manoj Pandey was born on March 28th 1980 in Lucknow, his hometown, somewhere in the north of India. He spent his childhood in various cities in India as his father, being in the Indian Air Force shifted every few years. In the process he got a flavor of different cities, towns and cultures, discovering little truth of life. Doing small experiments with water microscope , rubber band driven paddle boats , inventing perpetual motion machine led to the birth of scientific curiosity in him and he wanted to peruse it further.

After a fun filled high school experience at Kendriya Vidyalaya No. 2,Tambaram, he secured admissions to the Indian Institute of Technology at Chennai (then Madras) for his Bachelor's degree. During his Bachelor's he also visited Hochshule Bremen in Germany as an exchange student, where he worked on the numerical modeling of some life raft equipments. He obtained the degree of Bachelor of Technology in Naval Architecture and Ocean Engineering in July 2001.

After this he headed to distant lands as he was accepted into the department of Theoretical and Applied Mechanics at Cornell University in August 2001 for a Ph.D. He started his research on dynamics of MEMS with Professor Alan Zehnder, the following year. After a fruitful period of learning and experimentations he received his doctorate in January 2007 with a minor in Electrical Engineering.

To my parents

ACKNOWLEDGEMENTS

Ph.D. is a great learning experience and it requires collaboration with several people to reach its successful conclusion. I am thankful to some great individuals and institutions for providing this support and help during the course of this exciting journey.

Freedom is the most important thing while pursuing any kind of research and learning. Things may not workout at all times and it requires a big heart and foresight to continue working on a problem which might seem to be going no where. Hence I would like to extend my appreciations and gratitude towards the following for getting me past these phases.

I am grateful to my advisor, Professor Alan Zehnder for giving me ample freedom in choosing research topics and exploring new possibilities. He has been more than guide and like a parent and I am thankful to him for his tireless work on many of my writings as well on his ingenious suggestion at crucial times both pertaining to research and otherwise. Through constant mentoring he ensured my progress and success in the program.

I would like to thank Professor Richard Rand, for providing constant encouragement and support during the course of my Ph.D. His work ethics and his love for the subject is really infectious. I would always be indebted to him for extending help anytime I required it. Thanks are also due to Professor Amit Lal for some great suggestions and discussions on the research. Special thanks to Professor Subrata Mukherjee for his help and suggestions on the Finite Element Analysis.

I would also like to thank Robert Reichenbach for his immense contribution to the later part of this thesis. His help with fabrication of the dome resonators and setting up the experiments couldn't have come at a better time. Working with him

was a great experience and he is a great friend. I want to thank Professor Harold Craighead for his support to this project. I would also like to express my appreciation to Keith Aubin and Maxim Zalalutdinov for providing the experimental data and support for the work on entrainment. Thanks to Tuncay Alan for providing FEA data used in modeling of the disc oscillator. Thanks are also due to Shankar Radhakrishnan and Dana Weinstein for their help with CAD.

I would also like to thank Dan Mittler, Sreemati Mukherjee,Cindy Twardokus and Polly Marion for their help with administrative and computer support and making it a smooth sailing all the way.

I cannot thank enough, my friends for making this Ph.D. a great experience. Mahesh Shivashambhu for his guidance for the Ph.D. to which I came back to whenever I found myself lost. I am forever grateful to Anand Mohan Pappu, Abhishek Kammula, Peeyush Bhargava and Sovan Lal Das for their help on the research and other matters. Many thanks to Ishan Sharma, Pritam Ganguly, Tuhin Sahai, Pankaj Porwal, Vijay Murlidharan and Jayant Kulkarni who were not only great people to hang out with but also someone whom I learnt a lot from, both about work and life. Finally I want to thank Cornell Cricket team to keep me active and help me bounce back when the chips were down.

TABLE OF CONTENTS

LIST OF FIGURES

Chapter 1

Introduction

MEMS are micron sized mechanical structures typically made of silicon and/or its compounds and are used to replace complex electronic circuits in modern digital systems with improved performance and power requirement. These are specifically attractive in RF systems where they may be able to replace bulky off-chip components such as oscillators [5], filters, amplifiers, resonators, receivers etc. Other application include MEMS micromirrors,widely used in compact projectors and cinemas [6, 7]. MEMS inertial sensors (i.e., accelerometers and gyroscopes) have been successfully used in cars for safety, drive comfort and navigation [8]. They are also used in data storage devices [9].

Good mechanical properties of silicon and its abundant availability makes it an ideal material for MEMS. Silicon, which is an almost Hookean material has negligible hysteresis and other material losses associated with the motion. It is less susceptible to fatigue and hence could be used for several billions of cycles without failure. MEMS are manufactured using planar fabrication techniques compatible with preexisting integrated circuit(IC) fabrication technology, hence realizing systems where MEMS component provide specific high quality functions. Careful mechanical analysis is a key to the proper design of MEMS intended to achieve specific performance objectives.

1.1 Resonant MEMS

Resonant MEMS consist of devices whose function depends on the response close to the resonant frequency of the micro-mechanical structure. Such devices find

favor over the conventional electronic circuits in superheterodyne communication tranceivers [10], performing specialized functions such as electromechanical filters [11], amplifiers and non-linear mixers [12]. They also find use in different kinds of scanning probe microscopes [13, 14], as well as biological and chemical sensors [15], which use a change in the resonant frequency for detection.

Tunability is desirable for these devices as the information is carried by the resonant frequency. This is demonstrated by integrated tunable high Q filters and oscillators in telecommunication devices [16, 17]. These filters/oscillators offset the dependence on discrete and bulky crystal oscillators for frequency detection and tuning, significantly reducing the size and power consumption of the circuit. Broadband variable frequency micromechanical oscillators also find application in MEMS based spectrum analyzers. Similarly, tunable detectors are highly desired for magnetic resonance force microscopy (MRFM) applications.

Sensitivity and performance of these device depends on the sharpness of the resonant amplitude vs frequency response, defined in electronic systems by a parameter called quality factor, henceforth called the Q. Q^{-1} is a measure of the total loss in the system and is a sum of losses due to air damping, surface effects, material damping, thermo-elastic damping and clamping losses to the substrate. From the amplitude vs frequency response Q is determined as

$$Q = \frac{f_0}{\Delta f}$$

where f_0 is the natural frequency of the resonator while Δf is the bandwidth, or the maximum frequency width at the half power points or the frequency corresponding to the half the maximum energy stored in the resonator at the resonance. Figure 1.1 shows the above mentioned parameters on an amplitude-frequency curve.

A higher Q results in a sharper amplitude vs frequency response i.e. a smaller

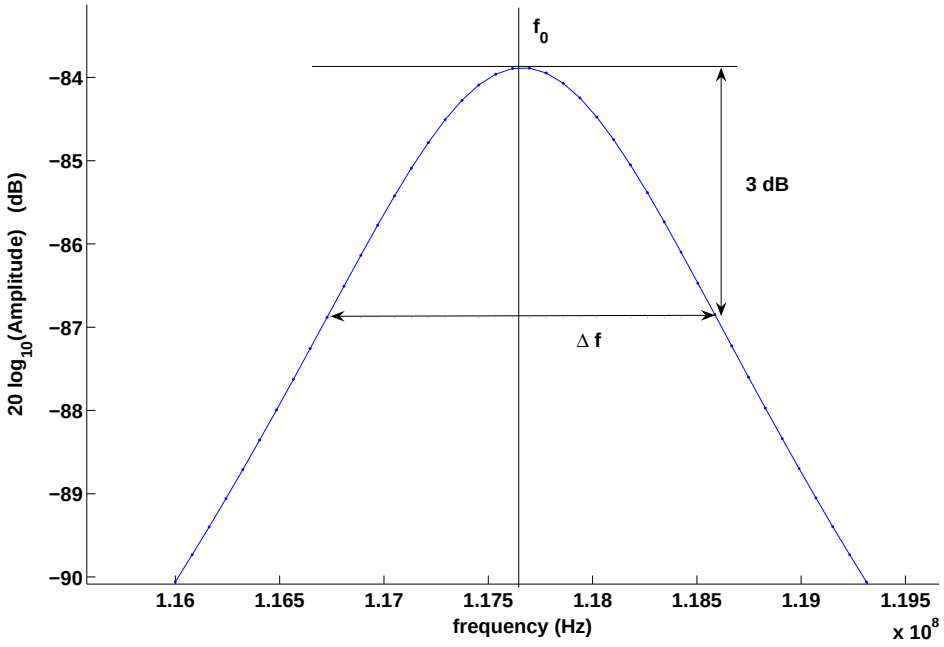

Figure 1.1: Various parameters shown on an amplitude-frequency curve, used to calculate Q of the resonator.

bandwidth, hence is desirable for better resolution in sensors. Higher Q in scanning force microscopy (SFM), results in better resolution of topography. Higher Q filters show better insertion loss, bandwidth, rejection and dynamic range [18–20]. Oscillators which are used in communication systems for frequency translation, synchronization or sampling applications also benefit from higher Q. It is important for the oscillators to have a stable resonant frequency against factors such as temperature fluctuations, aging, noise etc. The single most important factor affecting the stability is the Q. High Q MEMS resonators can be used in wireless systems as both the frequency generating and filtering elements. High Q automatically translates into low power consumption.

This work deals with mechanical/dynamical modeling of parametrically excited MEMS oscillators and resonators, specifically in capturing experimentally observed

phenomenon of frequency locking or entrainment for disc and dome shaped structures shown in Figures 1.2 and 1.3, hence providing them tunability. The resulting model helps in designing structures which can be used to improve the performance and quality of these devices. The optimum design is explored in the parameter space.

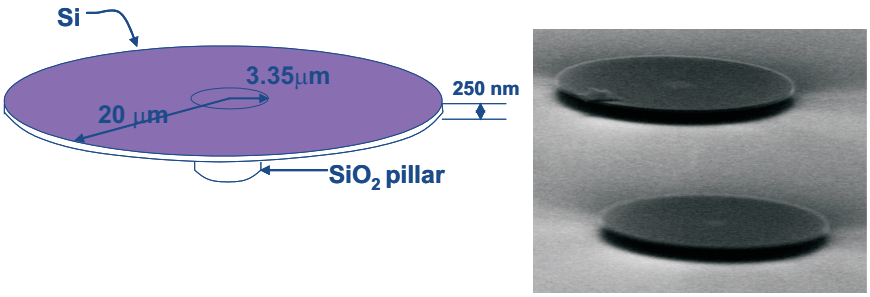

Figure 1.2: Disk-shaped oscillator. (right: SEM image of actual structure). From [1].

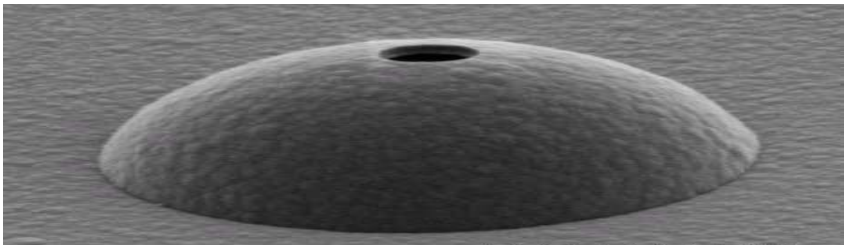

Figure 1.3: SEM image of dome-shaped oscillator.From [1].

1.2 Parametric Excitation and Entrainment

Entrainment is a phenomenon that can occur when periodic force is applied to a dynamical system whose free oscillation is self-excited, i.e. it vibrates even in the absence of external forcing. If the forcing is strong enough, and the frequency

difference between the forcing and the unforced oscillation is small, the response occurs at a multiple of the forcing frequency rather than at the natural frequency of the system. In such a case the response is said to be entrained by the forcing function and the system is said to be phase, or frequency locked. Thin, planar, radio frequency MEMS resonators have been shown to self-oscillate in the absence of external forcing when illuminated by a DC laser of sufficient amplitude [21]. In the presence of external forcing of sufficient strength and close enough in frequency to that of the unforced oscillations, the device will become entrained by the forcing and will vibrate at the frequency of the external forcing.

In the disk shaped oscillator to be described later, modulation of the absorbed laser energy leads to dynamic thermal stresses that change the stiffness of the device on time scales comparable to the period of vibrations [22]. When this occurs the oscillator is said to be parametrically excited. This term, "parametric excitation" stems from the time varying parameters of the differential equations that describe the motion of an oscillator. In contrast to the case of external excitation, where a small excitation cannot produce a large response unless the drive frequency is nearly resonant, small parametric excitation can produce a large response when the frequency of excitation is at certain integer ratios of the natural frequency of the system. Electrostatically driven parametric resonance in MEMS systems has been studied by Turner et al. [23, 24], Ruger and Grütter [25] and Carr et al. [26]. Parametric resonance in an electrostatically driven nanowire was observed by Yu et al. [27]. Ruger and Grütter point out that parametric drive can be used not only to amplify motion but to reduce thermomechanical noise as well, greatly increasing sensitivity of sensors built using parametric drive.

CW laser driven limit cycle oscillations were shown for MEMS resonators in the

shapes of disks [22], domes [21], paddles [28] and wires. Parametric amplification [29], entrainment [30], and operation in air [28] have been demonstrated. These devices usually are thin (100-250 nm) flexural or torsional structures suspended over a substrate.

A parametrically excited, coupled themomechanical model was developed for disk and dome shaped resonators [3]. Experimentally observed phenomena of limit cycle, frequency and phase entrainment were shown in this model using numerical integration of the governing equations [1, 2, 31]. In the present work the governing equations are studied using perturbation methods to determine various bifurcations leading to entrainment. Simpler canonical models with limit cycle can show behavior similar to the disk oscillator and hence provide simpler building blocks for the case when a large number of these device needs to be considered.

1.3 Clamping/Anchor Loss Minimization

Clamping/Anchor loss is a term used to describe the losses resulting from the leakage of energy from the resonator to the Si substrate via coupling through the clamps/anchors. Total damping of the resonator is the sum total of the various terms such as air damping, surface losses, thermo-elastic losses and phonon interaction. While air damping could be reduced by using these devices in vacuum, the surface losses could be reduced by surface treatment or annealing while thermo-elastic damping could be reduced by appropriate choice of material and dimensions. Losses to the substrate (clamping loss) still remain a large component of the total, especially at higher frequencies.

Few methods exist to reduce the clamping loss. In clamped devices clamping loss are inversely proportional to the frictional force, which is proportional to the

pressure on the clamps. Hence losses are reduced by increasing pressure on the resonators [32]. Clamping losses have been reduced by using flexible supports for clamped beams [33], essentially isolating the structure from the substrate. Clamping losses are reduced in systems with cantilevered supports by choosing the length of the support to be quarter wavelength of the resonant mode [34]. Improvement in Q of disk shaped MEMS in radial mode actuation is shown by Ngyuen [35] using hub modification, wherein the impedance mismatch between the hub and the disk is used to trap energy inside the disk.

In this work a design is presented to improve Q by reflecting the emanating waves towards the oscillator using a mesa structure. The energy hence reflected drives the resonator, in the process improving its Q for certain dimensions of the mesa. Such a design was first simulated using finite element analysis (FEA) which involved modeling relatively infinite substrate along with the resonator. Various techniques are explored to capture this effect. The results are verified experimentally for dome shaped resonators.

Chapter 2

Entrainment in a Disk Shaped Resonator

2.1 Introduction

Entrainment is the phenomenon in which freely oscillating systems synchronize with each other or with an external force. Entrainment can occur in numerous physical, chemical, biological and sociological systems. Examples of such systems include entrainment of human circadian rhythms by light, where the biological clock is entrained to the cycle of day and night [36], radio frequency systems [37], superconducting Josephson junction arrays [38] and the mutual entrainment of fireflies [39] which glow in unison after synchronization.

Here perturbation methods are used to analyze the entrainment behavior exhibited by a planar, disc-shaped micromechanical limit cycle oscillator. The oscillator, shown in Figure 1.2, consists of a thin circular plate of single crystal Si supported above a Si substrate by a SiO_2 pillar [22,30]. A constant (CW) laser beam, focused to a $5\mu m$ spot near the edge of the disc, is used both to detect the vibrations and to drive the disc. The disc is thin enough that much of the incident laser light is transmitted through the disc and then reflected back by the Si substrate below. This process repeats itself in a series of reflections and transmisions, the net result of which is that the disc-substrate system forms a Fabry-Perot interferometer. Both the net reflected and the net absorbed light vary periodically with the deflection of the disc at the point of illumination. Thus the laser can be used to interferometrically detect vibrations of the disc. In addition, the amount of heat absorbed and hence the thermal strains also vary with disc deflection. The oscillatory thermal strains produce a thermal drive of the disc and they modulate

the disc's stiffness [3]. Since the thermal driving force depends on the position of the disc, the system has feedback that can cause the rest position of the disc to become unstable when the laser power exceeds a threshold, driving the disc into limit cycle motions via a Hopf bifurcation [3].

In the experiments [30] the CW laser power was increased to a level just beyond the threshold for limit cycle oscillations. Once the disc was oscillating, it was found that the frequency of vibration can be tuned by applying a "pilot signal" consisting of either a modulation of the incident laser beam or an inertial drive provided by a modulated piezoelectric actuator taped to the back of the chip containing the disc. If the frequency of modulation of the pilot is close to the limit cycle frequency of the oscillator, the oscillator locks itself onto the pilot signal and remains locked in frequency and phase over a range of frequencies. The disc is said to have been entrained by the pilot signal. If the pilot frequency is not close to the oscillator limit cycle frequency, then the oscillator continues to oscillate at its own frequency and phase. The system exhibits hysteresis, that is, the entrainment region obtained when sweeping backward in frequency has different boundaries than the comparable region obtained when sweeping forward. The amplitude and frequency response for the case of inertial (piezo) pilot signal are shown in Figures 2.1 and 2.2. See [30] for further details of the experiments. Modeling of this device and numerical simulations of the governing equations have been discussed earlier in [1, 3, 40]. Here we use perturbation theory to discern additional details of the transitions into and out of entrainment that are not amenable to numerical simulations.

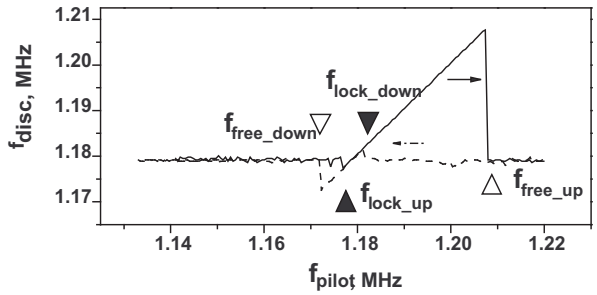

Figure 2.1: Frequency of response vs. piezo forcing frequency, obtained experimentally. From [2].

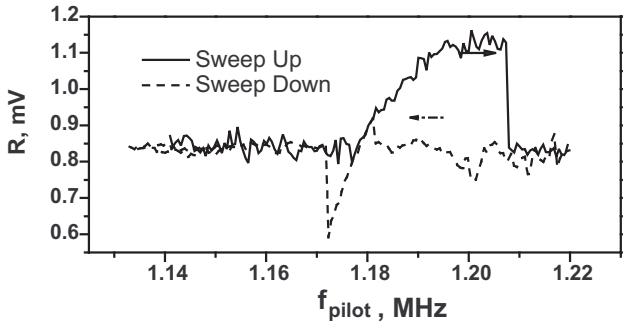

Figure 2.2: Amplitude of response vs. piezo forcing frequency, obtained experimentally. Amplitude shown as mV output from photodetector. Actual amplitude of motion is shown in [3] to range from 80-160 nm, or 0.13 to 0.26 λ, where λ is the wavelength of the incident light. From [2].

The model equations for this system are [1, 3]:

$$\ddot{z} + \frac{1}{Q}(\dot{z} - D\dot{T}) + (1 + CT)\Big(z - DT + \beta(z - DT)^3\Big) = M\sin(\omega_{piezo}t) \quad (2.1)$$

$$\dot{T} + BT = AP \ , \quad (2.2)$$

and

$$P = P_{laser}(1 + \varphi\cos(\omega_{\text{laser}}t))(\alpha + \gamma\sin^2(2\pi(z - z_0))). \quad (2.3)$$

where z represents the displacement of the disc at the location of the focused laser

beam and z_0 represents its equilibrium position. Both these quantities have been normalized by the wavelength of the incident light. T is the temperature of the disc. M represents the amplitude of the inertial (piezo) drive. P_{laser} is the CW laser power while φ is the amplitude of the AC laser signal. C is the relative change in spring constant per unit temperature change. D is the deflection of the disk due to heating, per unit temperature change. B represents the disk's overall thermal conductivity and A its overall thermal mass. β is the nonlinearity in the disk's stiffness. Time in equations (2.1)-(2.3) has been scaled by the natural frequency of the undamped linear oscillator and hence the natural frequency is 1. For a disc oscillator of outer diameter 35 μm and the inner diameter 7 μm that has a natural frequency of 1.2 MHz for the (0,0) mode, oscillating in vacuum, the parameters in the above equations are estimated to be [3]

$$\begin{aligned} &Q = 10000, \quad \beta = 0.4, \quad A = 0.0176^0 C/\mu W, \\ &B = 0.488, \quad C = 3.53 \times 10^{-4}/^0 C, \quad D = 1.3 \times 10^{-5}/^0 C, \\ &M = 0.000025, \quad \alpha = 0.06, \quad \gamma = 0.26, \quad z_0 = 0.064 \end{aligned} \tag{2.4}$$

It is to be noted that although eqations (2.1)-(2.3) involve two independent forcing frequencies, namely ω_{piezo} and ω_{laser}, we consider only scenarios in which these are applied one at a time. This is so because experimental results disucussed earlier in [1, 31] considered these cases for entrainment in actual MEMS devices.

We first summarize the motion predicted by the above system of equations. If the disc is heated with a continuous wave (CW) laser beam of power above the Hopf bifurcation threshold, a stable limit cycle of finite amplitude exists in the system [3]. If a modulated signal is also applied to the oscillator either in the form of inertial piezo drive or via a modulated laser beam, the system becomes

a nonautonomous one and the limit cycle becomes either a quasiperiodic motion, if the limit cycle and pilot signal frequencies are not close, or becomes a periodic motion at the pilot signal frequency if the frequencies are sufficiently close. If the laser power were to be switched off, so that the only forcing is coming from the piezo drive, then the system reduces to a forced Duffing oscillator and hence shows a backbone-shaped amplitude-frequency response [41].

2.2 Numerical Results

The numerical results for equations (2.1)-(2.3) are discussed extensively in [1]. Figure 2.3 shows the response amplitude vs. piezo forcing frequency for a case when P_{laser} is above the Hopf bifurcation threshold and hence the limit cycle exists. We look at the case of 1:1 entrainment of the disc by the piezo drive. For a frequency of 1.0 all the initial conditions lead to a limit cycle motion of amplitude around 0.25. The frequency response of the system is at the limit cycle frequency as seen from Figure 2.4.

As the forcing frequency is increased the limit cycle persists until a frequency of 1.008 at which the system jumps onto a lower amplitude motion, which occurs at a specific piezo forcing frequency. The disc is said to have been entrained by the forcing. It remains entrained until the forcing frequency reaches 1.045, during which its amplitude as well as its frequency increase steadily. After entrainment is lost the motion jumps back to the limit cycle. If the forcing frequency is swept backwards, the system stays on the limit cycle until a frequency of 1.012 where it is again entrained and remains so until a frequency of 1.005 when the system jumps back to the limit cycle. Since the region of entrainment while sweeping forward is different from the one sweeping back, we see hysteresis in the system. Similar

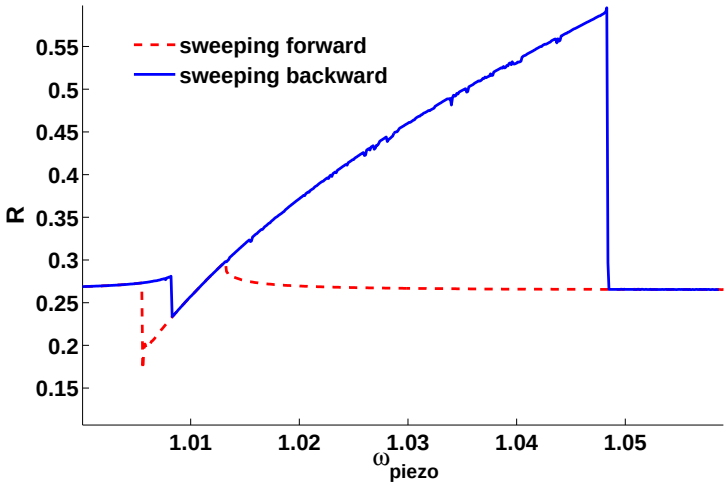

Figure 2.3: Amplitude of response vs. frequency of piezo drive, obtained by numerical integration of equations (2.1)-(2.3). M=0.0001, φ=0.0, P_{laser}=650μW for 1:1 piezo-modulation. From [1].

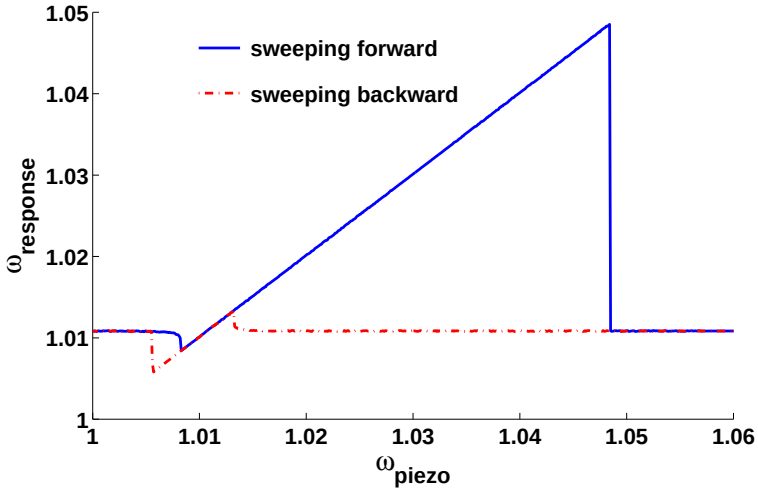

Figure 2.4: Frequency of response vs. frequency of piezo drive, obtained by numerical integration of equations (2.1)-(2.3). M=0.0001, φ=0.0, P_{laser}=650μW for 1:1 piezo-modulation. From [1].

behavior is seen when the laser beam is modulated with no piezo drive.

2.2.1 Effect of Changing Equation Parameters C & D

To study the effects of the parametric term $(1 + CT)$ and the optical drive term (DT) in the model equations, simulations are performed with $C = 0$ and $D = 0$.

First consider D=0, i.e. the effect of static deflection due to heating is neglected. For 2:1 laser modulation case, the system shows entrainment, although the amplitude drops down to zero while sweeping backwards when the entrainment is lost, Figure 2.5. Entrainment in this case is seen only at a very high value of CW laser power, 920 μW. This is because the Hopf bifurcation threshold increases as D decreases(see [40]). At higher laser powers the Hopf bifurcation changes to being super critical from sub critical. Thus an unstable limit cycle always exists between the stable limit cycle and the equilibrium. Hence if the amplitude during entrainment goes below the unstable limit cycle amplitude, it will drop to zero subsequently, when entrainment is lost, instead of jumping back to the stable limit cycle. Hence the results obtained by neglecting the D term in this case contradict the experimental observations.

For 1:1 piezo drive, if C=0, the model predicts that the disc will show the resonant behavior of a forced oscillator Figure 2.6. The limit cycle doesn't exist and entrainment is not predicted in this case which contradicts the experimental results. The same is the case for 1:1 laser drive.

Hence we see that optical drive term (DT) is important to model the system correctly.

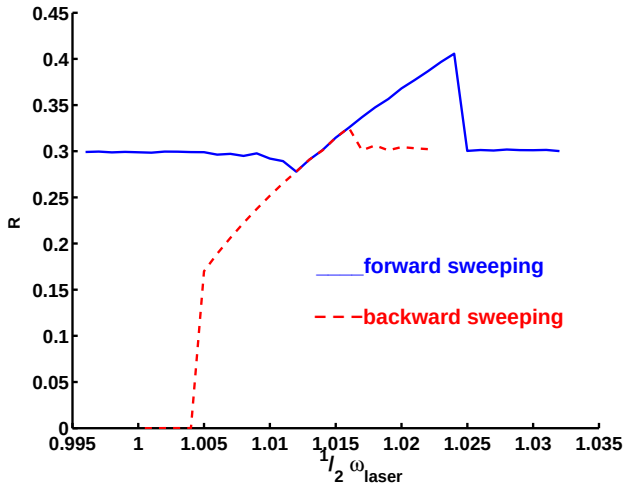

Figure 2.5: Amplitude response for 2:1 laser modulation case with D=0, M=0, φ=0.6, P_{laser}=920μW for 2:1 laser-modulation.

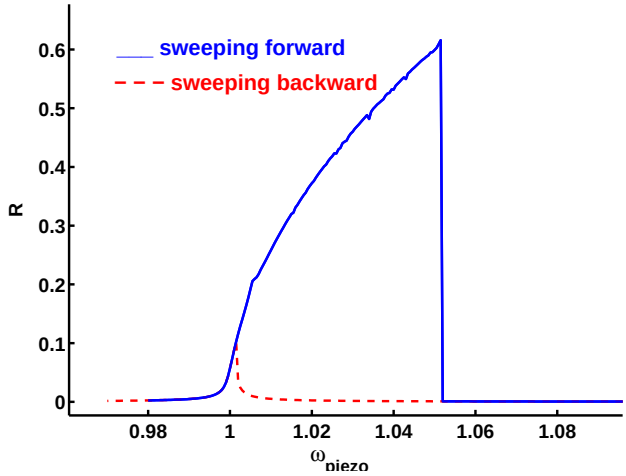

Figure 2.6: Amplitude of response vs frequency of piezo drive for D=0, M=0.0001, φ=0.0, P_{laser}=600μW for 1:1 piezo-modulation.

2.3 Perturbation Results

Two variable expansion perturbation method [41] is applied to the governing equations (2.1) and (2.3). This involves replacing time t by two time scales, stretched time $\xi = \omega t$ and slow time $\eta = \epsilon t$. Here ω is taken as the forcing frequency, that is, either $\omega = \omega_{\text{piezo}}$ or $\omega = \omega_{\text{laser}}$, depending upon which type of forcing we are considering. As mentioned earlier, examples in which both types of forcing are applied are not considered. To make the following analysis concrete, laser modulation is omitted by taking $\varphi = 0$ in equation (2.3), and choosing $\xi = \omega_{\text{piezo}} t$. The details of the method used are given in Appendix A.1. The result is a pair of slow flow equations which govern the evolution of the slowly varying coefficients $X(\eta)$ and $Y(\eta)$. Since these equations are very long if written out with all the parameters in unevaluated form, a version of the slow flow is presented instead which uses the numerical values of the coefficients listed in equation (2.4) and $P_{\text{laser}} = 650\mu W$:

$$\begin{aligned}
\dot{X} &= -M + a_{1,0}\,X + a_{0,1}\,Y \\
&\quad + a_{3,0}\,X^3 + a_{2,1}\,Y\,X^2 + a_{1,2}\,Y^2\,X + a_{0,3}\,Y^3 \\
&\quad + a_{5,0}\,X^5 + a_{4,1}\,Y\,X^4 + a_{3,2}\,Y^2\,X^3 + a_{2,3}\,Y^3\,X^2 + a_{1,4}\,Y^4\,X + a_{0,5}\,Y^5
\end{aligned} \tag{2.5}$$

$$\begin{aligned}
\dot{Y} &= b_{1,0}\,X + b_{0,1}\,Y \\
&\quad + b_{3,0}\,X^3 + b_{2,1}\,Y\,X^2 + b_{1,2}\,Y^2\,X + b_{0,3}\,Y^3 \\
&\quad + b_{5,0}\,X^5 + b_{4,1}\,Y\,X^4 + b_{3,2}\,Y^2\,X^3 + b_{2,3}\,Y^3\,X^2 + b_{1,4}\,Y^4\,X + b_{0,5}\,Y^5
\end{aligned} \tag{2.6}$$

where the numerical values of the coefficients $a_{i,j}$ and $b_{i,j}$ are given in Appendix A.2.

The slow flow equations can be used for an extended analysis of the original

system of equations at a much smaller computer budget. Much more information about the dynamical system could be obtained than is possible by using numerical integration. Fixed points of the slow flow (2.5),(2.6) correspond to periodic motions (limit cycles) in the original system, equations (2.1)-(2.3) [42]. Similarly, limit cycles of the slow flow correspond to quasiperiodic motions in the original system [42].

The numerical procedure can be summarized as follows: One of the fixed points of the slow flow (2.5),(2.6) is solved for numerically. Then using the continuation software AUTO [43], the locus of these fixed points is found as the detuning parameter k_1 is varied. Similarly the locus of all slow flow limit cycles can be obtained as a function of detuning. The resulting plot is shown in Figure 2.7. Phase plane plots are shown in Figure 2.8 for various regions in Figure 2.7. The following discussion is aimed at explaining the features of these figures.

Away from the resonance all initial conditions lead to motions which approach the limit cycle (labeled L). There exists an unstable slow flow fixed point close to the origin as well. The corresponding slow flow phase portrait is subfigure a) of Figure 2.8. As the forcing frequency is increased, the slow flow fixed point follows a backbone curve which corresponds to the associated Duffing oscillator (that is, to equation(2.1) with $C = D = 0$.) A saddle-node bifurcation occurs at the point labeled 56, and the phase portrait now looks like subfigure b). The stability of the fixed point following the resonance curve changes at the point labeled 54 where it becomes stable. The limit cycle (labeled L) meanwhile is stable and hence motion starting near it would continue to approach it during the forward sweep of frequency. The phase portrait here is shown in subfigure e). As the limit cycle

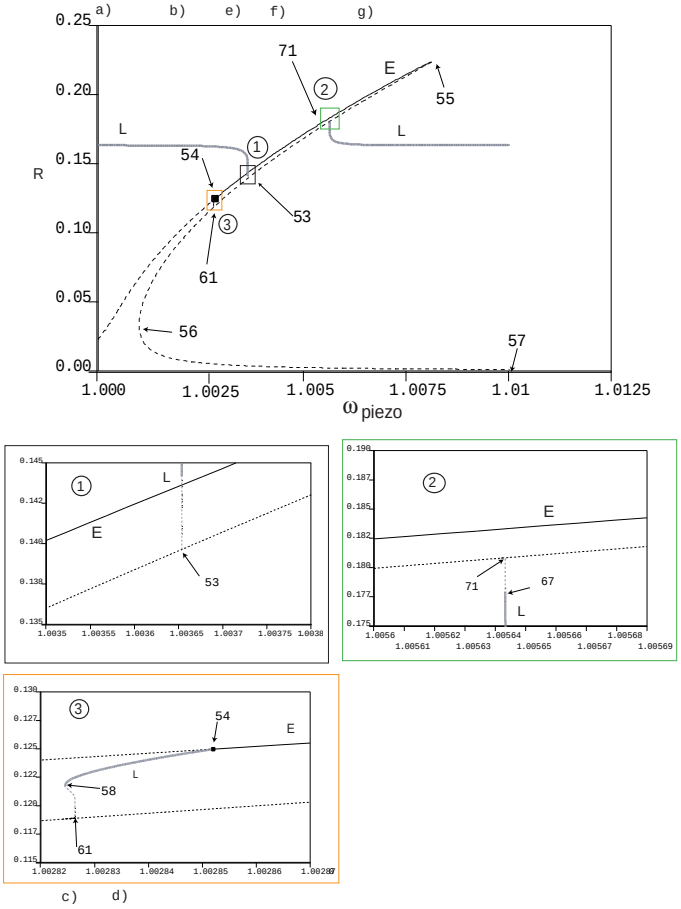

Figure 2.7: 1:1 Entrainment using piezo drive based on perturbation slow flow equations (2.5),(2.6). P_{laser}=650μW, $\varphi = 0$. 'L' denotes limit cycle in the slow flow, which corresponds to quasiperiodic motion in the original system (2.1)-(2.3), while 'E' is the entrained region which corresponds to stable fixed points in the slow flow. A solid line represents stable motion while a dashed line represents unstable motion. The insets contain close up views. Insets 1) and 2) show the disappearance of the limit cycle in a homoclinic bifurcation. Inset 3) shows how entrainment is lost while sweeping backward in frequency due to a supercritical Hopf bifurcation, see text. The letters a), b), ... mark the frequencies for which the phase portraits are shown in Figure 2.8.

approaches the resonance curve, its amplitude starts to decrease and close to point 53 its amplitude-frequency curve becomes vertical and loses stability. At this frequency only the slow flow fixed point is stable and the motion jumps to that. From the phase portrait plots we see that a homoclinic bifurcation takes place in the slow flow, wherein the limit cycle hits the saddle point and disappears i.e. going from e) to f) in Figure 2.8. This corresponds in the original system to a transition from quasiperiodic motion (a slow flow limit cycle) to a response at the forcing frequency (a slow flow equilibrium) and the system is said to have been entrained by the forcing. Increasing the forcing frequency beyond this point causes the system to continue on the locus of the stable fixed points of the system,which traces the backbone curve. At 71 a stable limit cycle is born from a homoclinic bifurcation and hence at ω= 1.0075 the phase portrait looks like subplot g). The motion however remains on the stable fixed point until point 55 where the stable fixed point and the saddle point disappear in a saddle-node bifurcation. The motion now jumps back to the stable slow flow limit cycle and the phase portrait again looks like a).

If the frequency is swept in the opposite direction, i.e. from high to low, the system at first stays on the stable slow flow limit cycle. This continues until point 71, where the limit cycle becomes unstable and the motion jumps to the nearby stable slow flow fixed point and the system is entrained. It should be noted that this point is lower in frequency than the point at which entrainment was lost in the forward sweep. This produces hysteresis in the system. The system traces the backbone curve until point 54 where the fixed point becomes unstable, undergoing a supercritical Hopf bifurcation in the slow flow. The corresponding phase portrait is shown in d). A stable slow flow limit cycle which was born in the Hopf bifurcation

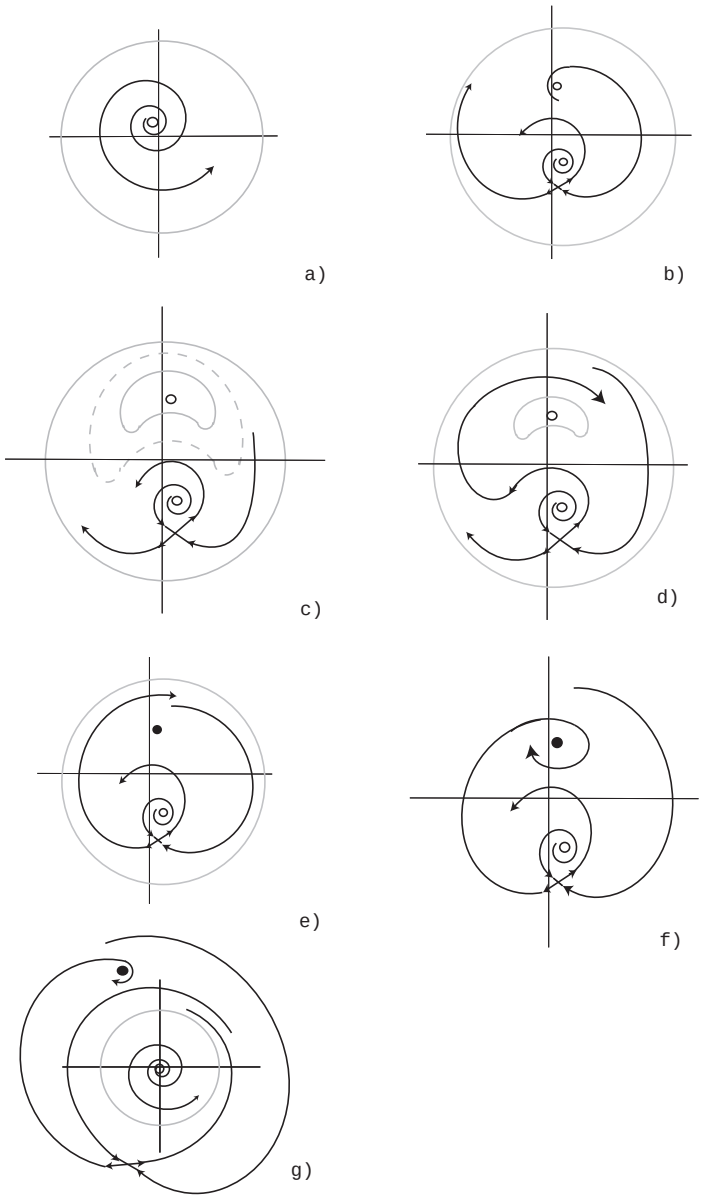

Figure 2.8: Phase portraits corresponding to Figure 2.7 at different frequencies. a) to the left of point 56 and to the right of point 55; b) between points 56 and 58; c) between points 58 and 61; d) between points 61 and 54; e) between points 54 and 53; f)between points 53 and 71; g) between points 71 and 55. Empty circles represent the unstable fixed points, filled circles the stable fixed points and closed orbits in lighter color the limit cycles in slow flow.

now surrounds the unstable fixed point. Another unstable limit cycle is born at 61 in a homoclinic bifurcation and the phase plane plot c) shows that it surrounds the stable limit cycle. These two slow flow limit cycles disappear in a cyclic fold bifurcation at point 58 shown in inset 3. The system now jumps back to the limit cycle L and entrainment is lost as the forcing frequency is decreased. The phase plane now looks like b). Decreasing frequency further causes the phase plane to again look like a) after a saddle-node bifurcation at point 56.

We note that equations (2.5), (2.6) and Figures 2.7, 2.8 apply to the system (2.1)-(2.3) which is driven by piezo forcing. We now consider the case in which the piezo drive is switched off and the system is driven by modulating the laser beam at close to twice the natural frequency of the unforced oscillator. We expect 2:1 resonance because of the parametric excitation involved in the term $(1+CT)\Big(z - DT + \beta(z-DT)^3\Big)$ of equations (2.1). Here T is periodic as shown in the foregoing discussion of the perturbation method, and provides the parametric excitation due to the $(1+CT)$ coefficient.

Figure 2.9 shows the results of a similar perturbation analysis for the case of 2:1 laser modulation forcing. The dynamics in this case are similar to the piezo driven case except that a subcritical Hopf bifurcation takes place at the point where the entrainment is lost as opposed to the supercritical Hopf bifurcation seen in the piezo forcing case.

Next the effect of switching off some of the terms in the governing equations is studied. Figure 2.10 shows the effect of turning off the C term, i.e. the parametric amplification term in equations (2.1). The slow flow limit cycle exists but with a smaller amplitude. It is seen that the slow flow limit cycle is born and continues from the point where the fixed point changes its stability, undergoing a Hopf

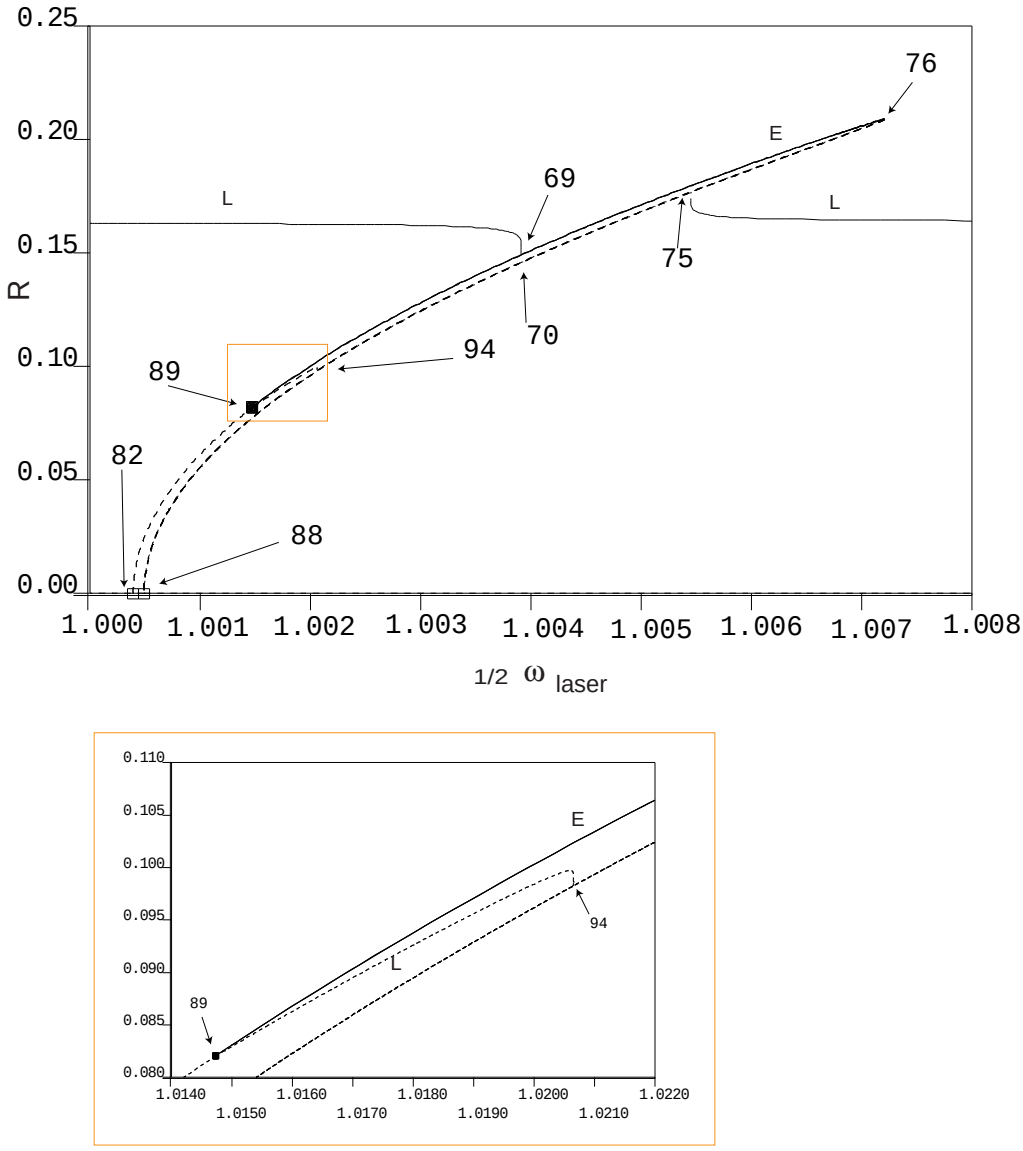

Figure 2.9: Entrainment using laser modulation from a perturbation slow flow analysis. P_{laser}=650μW and M=0. The inset contains a closeup near the frequency at which entrainment is lost sweeping backwards due to a subcritical Hopf bifurcation.

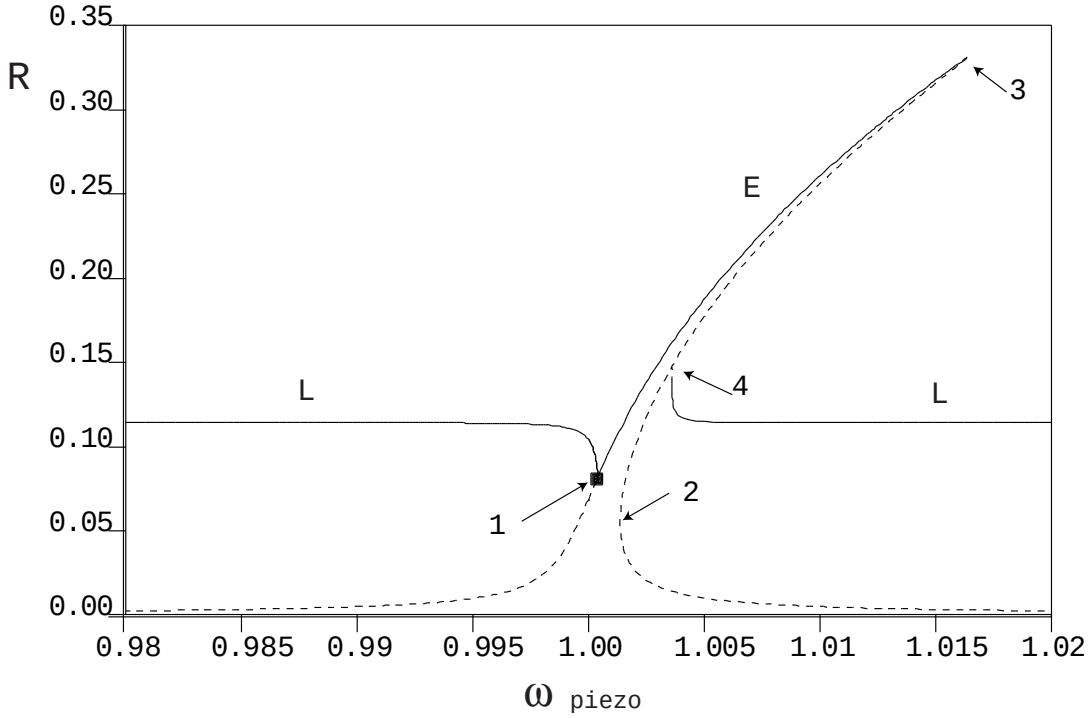

Figure 2.10: Entrainment region for piezo forcing with C=0, from a perturbation slow flow analysis. P_{laser}=650μW and φ=0. 'L' denotes the limit cycle in the slow flow while 'E' is the entrained region which corresponds to a stable fixed point of the slow flow. These results contradict the observed experimental results, showing that the C term is needed to correctly model the physical system.

bifurcation (labeled 1 in Figure 2.10). Hence the point where the entrainment is lost while sweeping backwards in frequency is the same as the point at which the system gets entrained while sweeping forward. This behavior contradicts that of the physical system as shown in Figure 2 and 3. Similar behavior, namely that there is no hysteresis and the amplitude is lower when C=0, was seen in the numerical integration of original equations in [1]. Hence the C term is needed to correctly model the physical system.

Removing the effect of heating on the deflection of the disk, i.e. setting D = 0, results in the slow flow simulation shown in Figure 2.11 for a laser power of 1650 μW. At the laser power of 650 μW (not shown) the system exhibits only the resonant behavior of a Duffing Oscillator [41], as the slow flow limit cycle doesn't exist in the system at this power. It was shown in [3, 40] that taking $D \to 0$ pushes the Hopf bifurcation threshold to a very high value. Hence the limit cycles exist only for very high laser powers and there exists an unstable limit cycle of smaller amplitude along with the stable one. The amplitude frequency curve in Figure 2.11 is explained next. While sweeping forward in frequency, the motion would exist on the stable slow flow limit cycle and would become entrained at the point marked 8. It would remain entrained until the point 5, after which it jumps down onto a slow flow limit cycle again. While sweeping backwards, the limit cycle would entrain at point 4. It remains entrained until point 2 where the fixed point becomes unstable and a stable limit cycle is born from a Hopf bifurcation. This limit cycle disappears just like in the case of Figure 2.7, due to a cyclic fold bifurcation. The motion then jumps down to the resonance curve at point 9. Further decreases in forcing frequency produce a jump up onto the resonance curve at point 6. Here there are two stable slow flow states, a stable equilibrium and a stable limit cycle. Their basins of attraction are separated by an unstable limit cycle. After this, the system follows the resonance curve and the amplitude dies out as frequency decreases. Similar behavior was seen in the numerical simulations [1]. The perturbation theory results and the numerical results predict behavior that contradict the observed experimental results, showing that the D term is needed to correctly model the physical system.

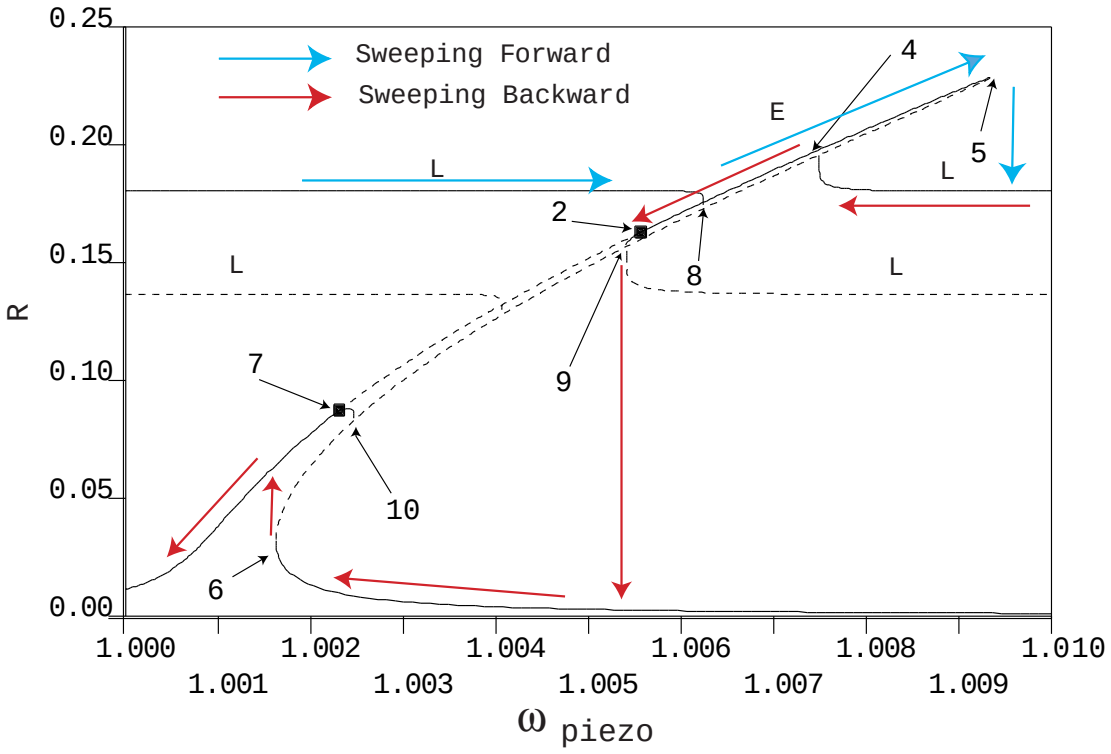

Figure 2.11: Entrainment region for piezo forcing with D=0, from a perturbation slow flow analysis. P_{laser}=1650μW and φ=0. Solid lines represent stable motion while dashed lines represent unstable motion. 'L' denotes a limit cycle in the slow flow while 'E' is the entrained region which corresponds to a stable fixed point of the slow flow. These results contradict the observed experimental results, showing that the D term is needed to correctly model the physical system.

Chapter 3

Simpler Models for Entrainment

Entrainment studied in the previous chapter involved constructing a model for the disc resonator from the experimental observations and careful finite element simulations. The resulting system of equations forms a three dimensional system of equations requiring large computational resources to obtain the response. In this chapter it is shown that the essential features of entrainment seen in the disc resonator can be captured by a combination of simpler canonical equations. The simpler model helps in understanding various symmetries in the parameters.

The following are the essential features of the entrainment in disc resonator:

- For DC laser of sufficient power disc resonator starts to self oscillate at constant amplitude. The simplest canonical model which captures this behavior is a van der Pol oscillator [42]. It consists of an $-\epsilon\dot{x}(1-x^2)$ term added to a 1D simple harmonic oscillator(SHO), which in the absence of forcing, leads to a steady state vibration called a limit cycle. For small values of ϵ the limit cycle has frequency close to 1, which is the frequency of the unforced linear oscillator.

- The limit cycle in the system can be forced either parametrically by modulating the laser or nonparametrically using a peizo drive. Mathieu equation term [42], $(1+\epsilon\alpha\cos(2\omega t))x$, can model parametric forcing of the system applied at twice the natural frequency of the resonator. This term in the absence of the vdP term, renders the origin unstable when the parametric forcing frequency 2ω is close to twice the frequency of the unforced linear oscillator. Nonparametric forcing can be modeled by a term of form $F_0\sin\omega t$.

- When entrained the system shows a backbone shaped amplitude vs forcing frequency response. This kind of behavior is typical of large amplitude response of structures and can be modeled by a Duffing's equation term [42], $\epsilon\beta x^3$, added to the SHO.

3.1 Entrainment in a Van der Pol Duffing System

We study the following equation:

$$\ddot{x} + x - \epsilon\dot{x}(1 - x^2) + \epsilon\beta x^3 = \epsilon F \ \cos\omega t \tag{3.1}$$

where ϵF is the magnitude of nonparametric forcing applied at frequency ω and β is the coefficient of the cubic nonlinearity term. ϵ is a small parameter which will be used in the perturbation method. Eq.(3.1) is a combination of van der Pol (vdP) and Duffing's equation term to the forced Harmonic oscillator. Looking ahead, we may expect eq.(3.1) to exhibit the following two types of dynamical behavior:

- A quasiperiodic motion corresponding to the two frequencies of a) the limit cycle , and b) the forcing terms. This case is expected if the forcing amplitude is too small to produce entrainment.

- A periodic motion if the forcing amplitudes are sufficiently large. 1:1 resonance occurs if the forcing frequency, ω, is close to 1. The system is said to have been entrained by the forcing frequency.

3.2 Numerical Simulations

As expected, the numerical results in Figure 3.1 show that away from the resonance i.e. for k_1 away from 1, the response consists of a quasiperiodic motion, which is a combination of the limit cycle and a small contribution from the forcing. As the frequency is swept the constant amplitude motion suddenly jumps onto a single frequency response which increases in amplitude with a further increase in the forcing frequency. Beyond a certain forcing frequency the motion jumps back to the lower amplitude limit cycle response. Hysteresis is seen when the frequency is swept back.

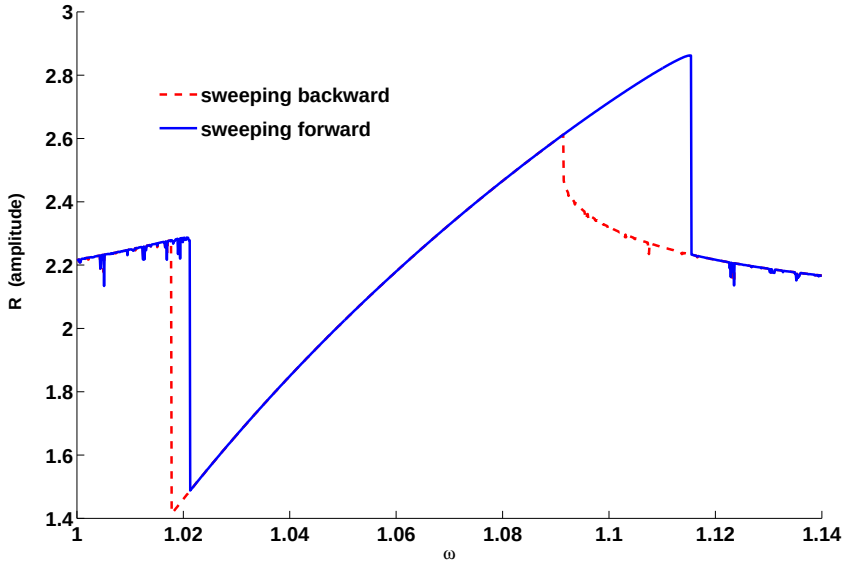

Figure 3.1: Steady state solution obtained by numerical integration of equation 3.1 . F=3.0, β=3.75 and ϵ=0.1.

3.3 Perturbation Scheme

In order to better understand the foregoing numerical results, and to study the effect of changing parameters, we use the two variable expansion method (also known as the method of multiple scales) to obtain an approximate analytic solution. The idea of this method is to replace time t by two time scales, $\xi = \omega t$, called stretched time, and $\eta = \epsilon t$, called slow time. The forcing frequency ω is expanded around the natural frequency of the oscillator (ω= 1), i.e.

$$\omega = 1 + k_1\epsilon + O(\epsilon^2) \tag{3.2}$$

where k_1 is a detuning parameter at order ϵ. Next, x is expanded in a power series in ϵ:

$$x = x_0(\xi, \eta) + \epsilon x_1(\xi, \eta) + O(\epsilon^2) \tag{3.3}$$

Substituting (3.2),(3.3) into (3.1) and collecting terms gives:

$$x_{0\xi\xi} + x_0 = 0 \tag{3.4}$$

$$x_{1\xi\xi} + x_1 = -2k_1 x_{0\xi\xi} + (1 - x_0^2)x_{0\xi} + \beta x_0^3 + F\cos\xi \tag{3.5}$$

We take the solution to eq.(3.4) in the form:

$$x_0(\xi, \eta) = A(\eta)\ \cos\xi + B(\eta)\ \sin\xi \tag{3.6}$$

Substitution of (3.6) into (3.5) and removal of secular terms gives the following slow flow:

$$\dot{A} = \frac{AB^2}{8} + \frac{A^3}{8} - \frac{A}{2} - Bk_1 + \frac{3}{8}B^3\beta + \frac{3}{8}A^2B\beta \tag{3.7}$$

$$\dot{B} = \frac{B^3}{8} + \frac{A^2B}{8} - \frac{B}{2} - Ak_1 + \frac{F}{2} + \frac{3}{8}AB^2\beta + \frac{3}{8}A^3\beta \tag{3.8}$$

3.4 Perturbation Results

Figure 3.2 shows the perturbation results for the equations 10 and 11. As expected,

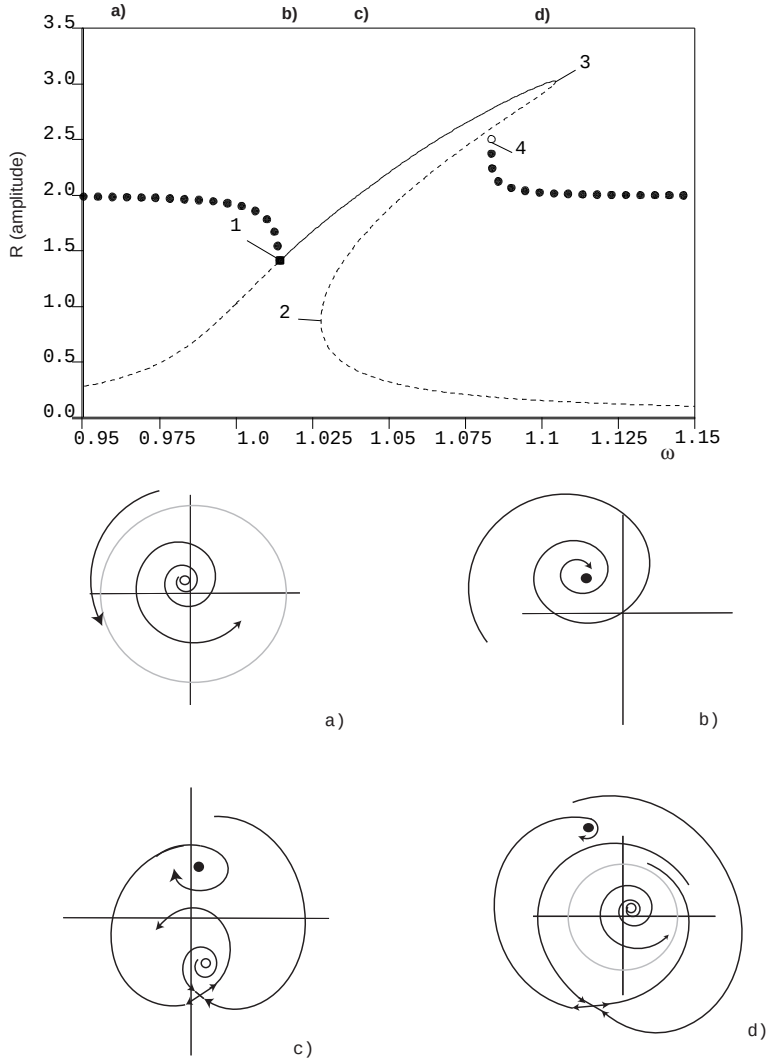

Figure 3.2: Perturbation results obtained by continuation of the results for equations 3.7, 3.8. F=3.0, β=3.75 and ϵ=0.1.

away from the resonance a limit cycle is seen to coexist with an unstable fixed point, which is close to zero. As the forcing frequency gets closer to the resonant frequency, the unstable fixed point increases in amplitude and undergoes subcritical

Hopf bifurcation at point 1, becoming a stable fixed point in the process. The stable limit cycle disappears at this point and the motion jumps onto the stable fixed point. The system is now entrained by the forcing and it follows the resonance curve of the Duffing oscillator, increasing in amplitude all the while until point 3. A saddle point arises at point 4 from a saddle node bifurcation and has amplitude close to but lower than the mentioned stable fixed point of the resonance curve. The stable fixed point disappears next in a saddle node bifurcation with the saddle point, close to the resonance curve at point 3. The motion then jumps back to the limit cycle with further increase in forcing frequency. When the frequency is swept back, it is clear that the point at which the limit cycle would be entrained must be different from the point at which the resonance curve disappears. The entrainment in this case is achieved when the limit cycle undergoes a fold and hence the motion jumps back to the stable fixed point at 4. The system then follows the resonance curve until the Hopf bifurcation point 1. Hysteresis is seen in the extent of the entrainment region depending on the direction of sweep. The phase plane plots associated with different regions are also shown.

Figure 3.3 shows the effect of changing the parameter β on the entrainment region. In addition to the increasing slope of the resonance curve, increasing β causes Hopf bifurcation to become subcritical from a supercritical one, as seen in subfigure (c). The unstable limit cycle annihilates with the stable limit cycle, undergoing a fold at point 4. This has an effect on the entrainment region as the limit cycle doesn't entrain at the Hopf bifurcation point as before and jumps onto the stable fixed point at the frequency corresponding to the fold instead. The point of losing the entrainment while sweeping back still remains the same i.e. the Hopf bifurcation point. Hence this also contributes to the hysteresis. Increasing

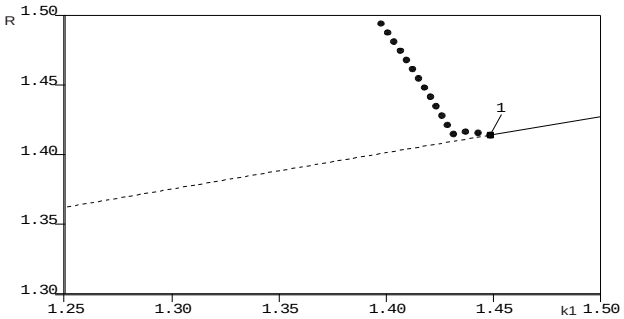

a)

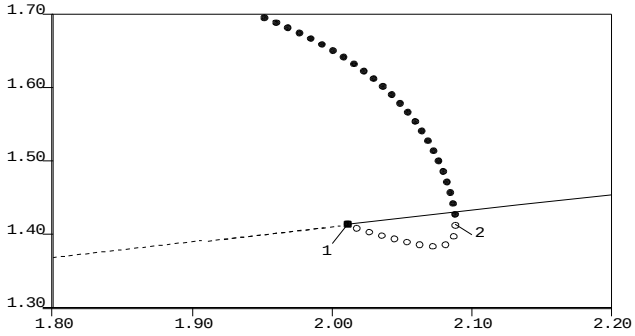

b)

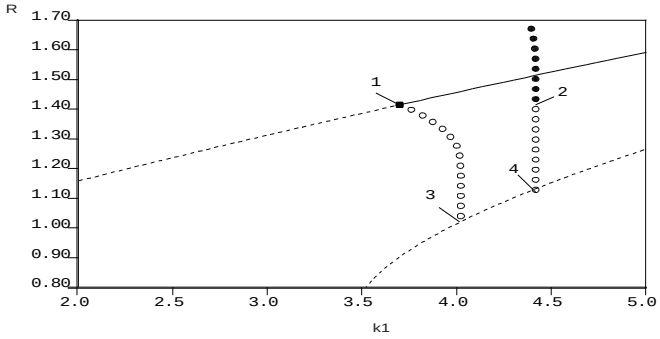

c)

Figure 3.3: The approach to entrainment region as a function as β is varied. a) β = 3 b) $\beta = 3.75$ c) $\beta = 6.0$.

β further causes the limit cycle amplitude to get closer to the saddle point until two distinct branches of the unstable limit cycles are seen. One originates from the Hopf and the other originating from the fold. Both these unstable limit cycles hit the saddle fixed points and disappear in a homoclinic bifurcation. This figure looks very similar to the MEMS system studied in the previous works [44].

3.5 Entrainment in a Mathieu Van der Pol System

Next the following differential equation, which may be thought of as a forced Mathieu-van der Pol equation is studied:

$$\ddot{x} + (1 + \epsilon\alpha \ \cos(2\omega t + \phi))x - \epsilon\dot{x}(1 - x^2) = \epsilon F \ \cos\omega t \tag{3.9}$$

where $\epsilon\alpha$ is the magnitude of parametric forcing applied at frequency 2ω, and ϵF is the magnitude of nonparametric forcing applied at frequency ω while ϕ is the phase difference between the parametric and the nonparametric forcing. ϵ is a small parameter which will be used in the perturbation method. Eq.(3.9) combines Mathieu equation term to the forced van der Pol equation. This adds parametric forcing to the system.

Looking ahead, we may expect eq.(3.9) to exhibit the following two types of dynamical behavior:

- A quasiperiodic motion corresponding to the two frequencies of a) the limit cycle , and b) the forcing terms. This case is expected if the forcing amplitude is too small to produce entrainment.

- A periodic motion if the forcing amplitudes are sufficiently large. This could result from either 1:1 resonance if the nonparametric forcing frequency, ω,

is close to 1, and/or 2:1 subharmonic resonance if the parametric forcing frequency, 2ω, is close to 2.

3.6 Numerical Integration

We begin by numerically integrating eq.(3.9) and displaying the results in Figure 3.4, which shows the response amplitude as a function of forcing frequency ω for parameters $\epsilon = 0.1$, $\alpha = 1$, $F = 0.3$ and $\phi = 0$. Quasiperiodic behavior (QP) is observed in the regions located approximately at $\omega < 0.97$ and $\omega > 1.03$. Periodic behavior at the forcing frequency is observed in the rest of the plot, corresponding to entrainment. As we sweep the frequency forward inside the entrained region, the amplitude jumps to a higher value at a frequency $\omega \approx 1.015$. No comparable jump is seen when the frequency is swept backward, indicating hysteresis.

3.7 Slow Flow

Using perturbation scheme similar to the previous section following slow flow is obtained:

$$A' = -k_1 B + \frac{A}{2} - \frac{A}{8}(A^2 + B^2) - \frac{\alpha}{4}(A\sin\phi + B\cos\phi) \tag{3.10}$$

$$B' = k_1 A + \frac{B}{2} - \frac{B}{8}(A^2 + B^2) + \frac{\alpha}{4}(-A\cos\phi + b\sin\phi) + \frac{F}{2} \tag{3.11}$$

3.8 Invariances of the slow flow

The slow flow (3.10),(3.11) contains 4 parameters: detuning k_1, parametric forcing amplitude α, nonparametric forcing amplitude F and the phase difference ϕ. We shall be interested in understanding how the phase portrait of the slow flow

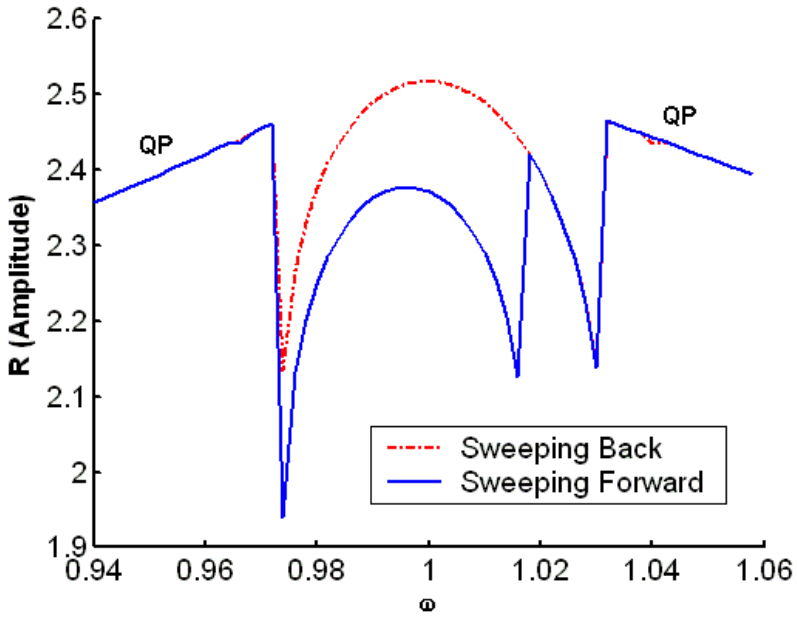

Figure 3.4: Results of numerical integration of equation 3.9 for parameters $\epsilon = 0.1$, $\alpha = 1$, F = 0.3 and $\phi = 0$. Response amplitude R is plotted against forcing frequency ω. Quasiperiodic behavior (QP) is observed in the regions located approximately at $\omega < 0.97$ and $\omega > 1.03$. Periodic behavior at the forcing frequency is observed in the rest of the plot, with hysteresis as shown.

is determined by these parameters. However, before discussing this we note that eqs.(3.10),(3.11) exhibit some invariances which permit useful conclusions to be drawn. For example, eqs.(3.10),(3.11) remain unchanged when A, B and F are replaced respectively by $-A$, $-B$ and $-F$. Since such a change does not alter the nature of the phase portrait, we see that *we may consider* $F \geq 0$ *without loss of generality.*

In addition, we see that Equations (3.10) and (3.11) remain unchanged when A, k_1, α and ϕ are replaced respectively by $-A$, $-k_1$, $-\alpha$ and $-\phi$. Since changing

the sign of A does not alter the nature of the phase portrait, we see that *we may consider* $\alpha \geq 0$ *without loss of generality* since negative α just reverses the k_1 and ϕ axes in the $k_1 - F - \phi$ bifurcation diagram, which leaves it essentially unchanged.

By the same reasoning, we may consider $\phi \geq 0$ without loss of generality, since replacing ϕ by -ϕ leaves the $k_1 - F - \alpha$ bifurcation diagram essentially unchanged. However since eqs.(3.10),(3.11) are 2π-periodic in ϕ, we may equally well choose ϕ to lie in any interval of length π. *Hence we may consider* $-\frac{\pi}{2} < \phi < \frac{\pi}{2}$ *without loss of generality.*

3.9 Parametric Study

In order to understand how the dynamical behavior varies as k_1, α, F and ϕ are changed, we used the AUTO bifurcation software package [43].

Figure 3.5 shows the results of the AUTO analysis for $\alpha = 1$ and $\phi = 0$, where k_1 and F are varied . Region A contains 5 slow flow equilibria, consisting of 2 sinks, 2 saddles and 1 source, i.e., only 2 are stable. These stable equilibria correspond to frequency locked periodic motions in equation (3.9). The presence of two such steady states signals the possibility of hysteresis. This same (stable) steady state occurs in region D, which lies above region A in Figure 3.5. The difference between these two regions is that D contains only 3 slow flow equilibria, namely 2 sinks and a saddle. As we cross the curve separating A and D, two of the saddles in A merge with the source in A in a pitchfork bifurcation, leaving a single saddle in their place.

We next consider regions E and B which lie to the left and right of region A

in Figure 3.5. The slow flow phase portrait for points in these two regions are qualitatively the same, consisting of 3 slow flow equilibria, namely a source, a saddle and a sink. Only one of these slow flow equilibria is stable, and corresponds to a periodic motion at the forcing frequency in equation(3.9). This same (stable) steady state occurs in region C_2, which lies above region D in Figure 3.5. The difference between region C_2 and regions E and B is that C_2 contains just 1 slow flow equilibrium point, namely a sink.

As we cross the curve separating C_2 from one of the regions E, D or B below it (each of which contains 3 slow flow equilibria), a saddle-node bifurcation occurs leaving a single sink in region C_2.

We have now discussed all regions in Figure 3.5 except for regions C_1 which lie in the lower left and right portions of Figure 3.5. Regions C_1 contain a single unstable slow flow equilibrium point, namely a source. However, unlike the other regions in Figure 3.5, regions C_1 also contain a stable slow flow limit cycle. This motion corresponds to a stable quasiperiodic motion in equation(3.9). Hopf bifurcations occur along the curves separating regions C_1 and C_2.

We offer the following summary of predicted (stable) steady state behavior of equation(3.9): In regions A and D we have 2 distinct stable periodic motions; in regions E, C_2 and B we have a single stable periodic motion; and in regions C_1 we have a stable quasiperiodic motion.

The discussion thus far has fixed α at unity (Figure 3.5). We next look at the effect of changing α. See Figure 3.6. We see that the width of the region corre-

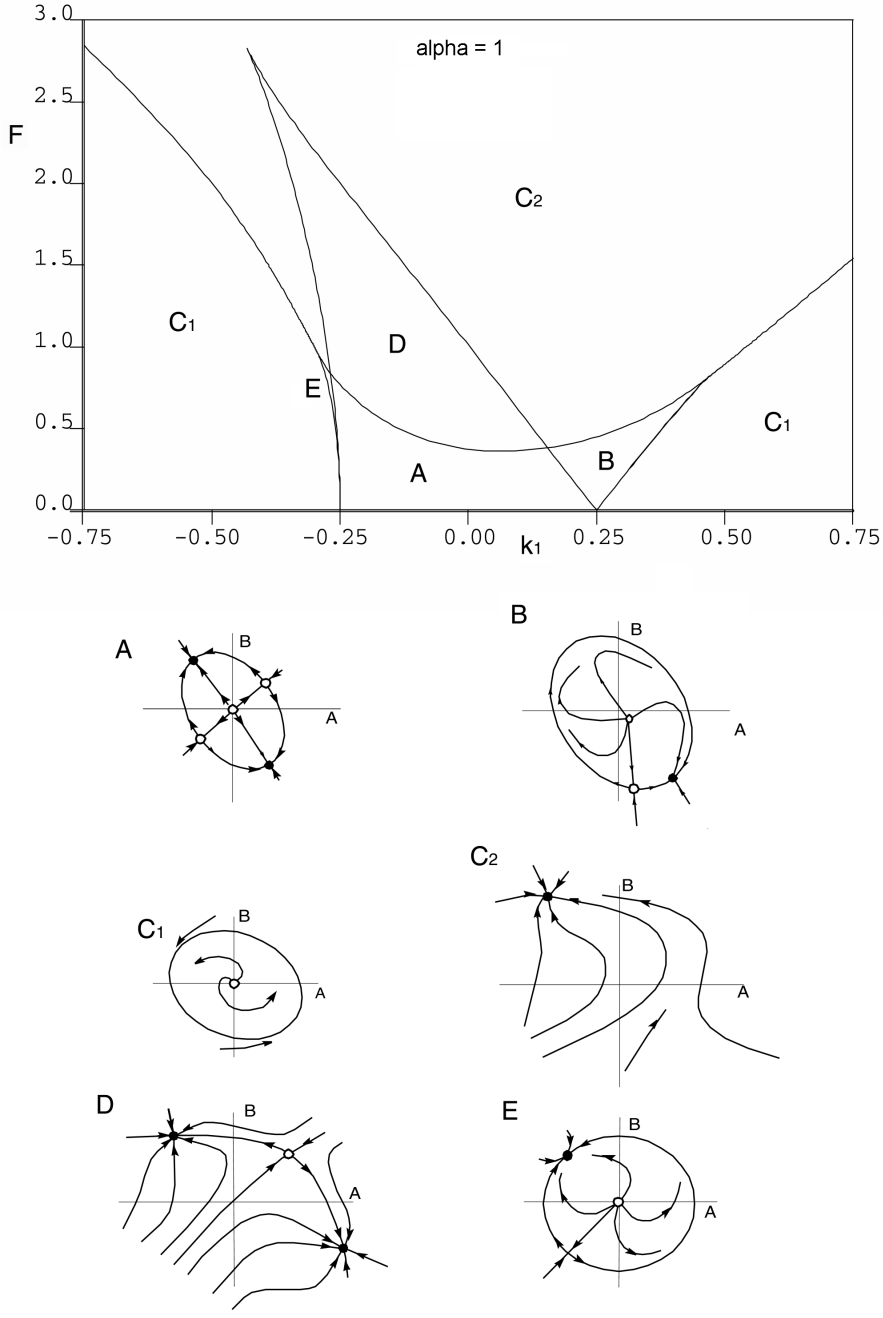

Figure 3.5: Behavior of the slow flow (7),(8). Bifurcation curves (obtained using AUTO) and sketches of corresponding slow flow phase portraits are displayed for $\alpha = 1$ and $\phi = 0$.

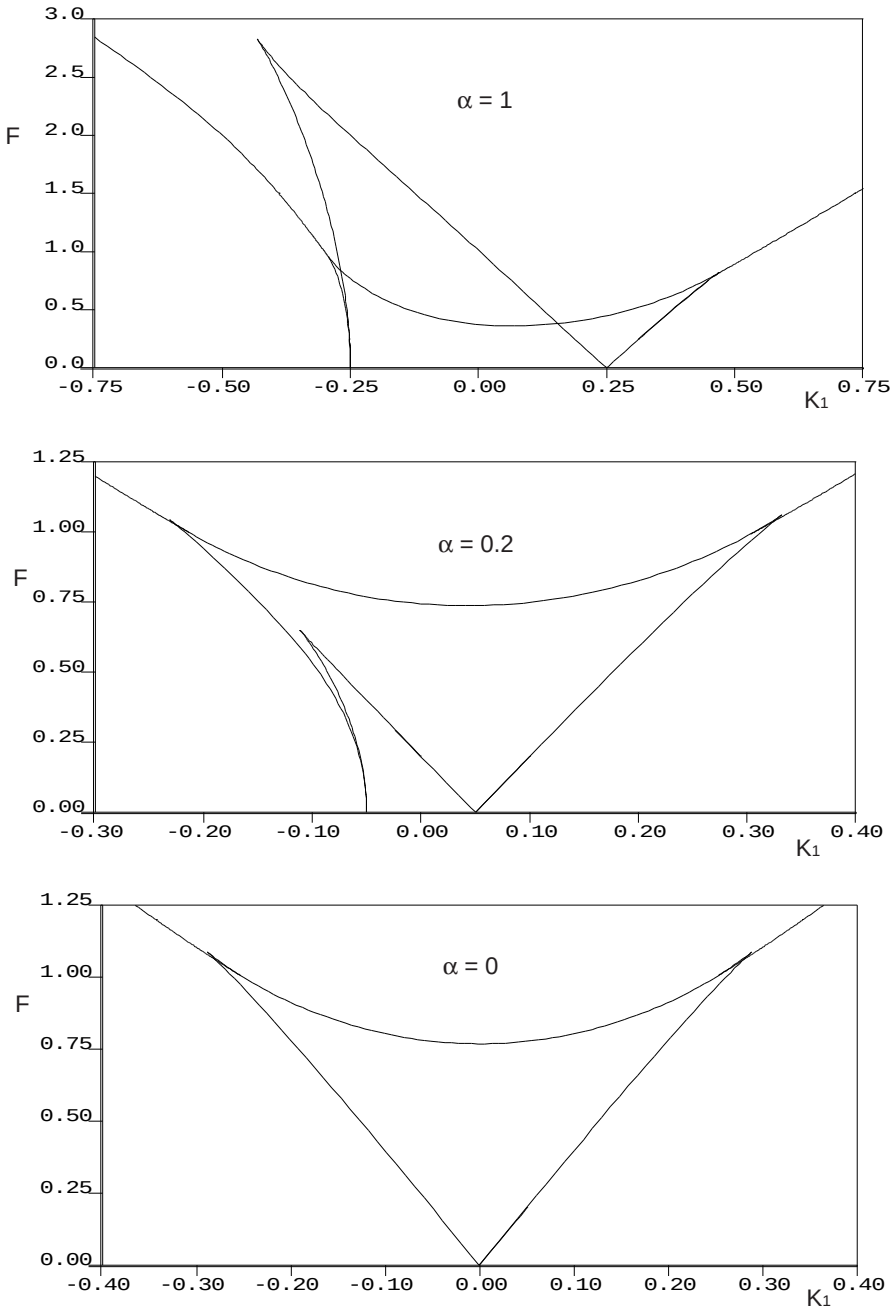

Figure 3.6: Bifurcation curves (obtained using AUTO) for slow flow (7),(8), for α = 1, 0.2 and 0.$\phi = 0$ in all the cases.

sponding to 2 distinct steady state periodic motions (regions A and D) decreases as we decrease α. In addition the regions B and E become more symmetrical. For $\alpha = 0.2$ we see that the region D has disappeared and the regions E and B have merged to give just one region. At $\alpha = 0$ the region with 2 stable steady states has disappeared. This case corresponds to nonparametric periodic forcing of a van der Pol oscillator, and has been discussed in [41].

Thus the presence of the regions A and D which contain 2 stable periodic motions may be associated with the parameter α. Since α is the coefficient of the parametric excitation term which has frequency 2ω, we may associate these regions with 2:1 subharmonic response. This is in contrast to regions E, B and C_2, which may be associated with 1:1 frequency locking.

The dependence of the bifurcation curves of Figure 3.5 on ϕ is displayed in Figure 3.7. The diagram is seen to be symmetric about $k_1 = 0$ for $\phi = \frac{\pi}{2}$ and $\phi = -\frac{\pi}{2}$. As long as the nonparametric forcing leads the parametric forcing (i.e. $-\frac{\pi}{2} < \phi < 0$), decreasing phase magnitude $|\phi|$ bends the region of 2:1 entrainment (regions A and D) to the left. As a result, region E becomes very small for $\phi = 0$. On the other hand when the parametric forcing leads the nonparametric forcing (i.e. $0 < \phi < \frac{\pi}{2}$), increasing ϕ causes region E to increase in size at the expense of region D, until at $\phi = \frac{\pi}{2}$ region D completely disappears and the region E is the same size as B. For values of ϕ in the range $[\frac{\pi}{2}, \frac{3\pi}{2}]$, the $k_1 - F$ bifurcation diagram is essentially the same as shown in Figure 3.7 , as discussed earlier in the section on invariances of the slow flow.

In conclusion, simplified canonical models were studied for entrainment behav-

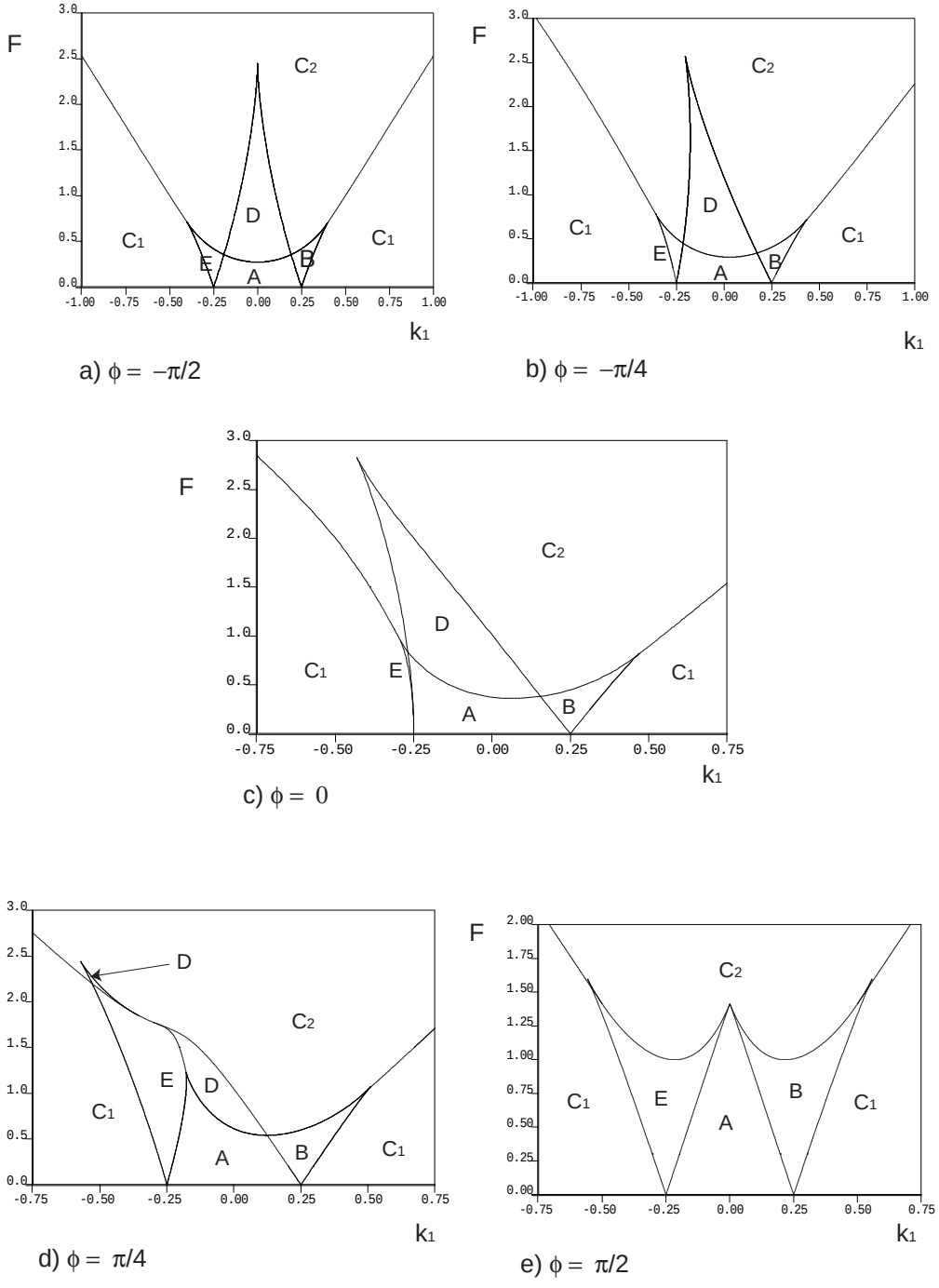

Figure 3.7: Bifurcation curves (obtained using AUTO) for slow flow (7),(8), for $\phi = \frac{-\pi}{2}, \frac{-\pi}{4}, 0, \frac{\pi}{4}$ and $\frac{\pi}{2}$. $\alpha = 1$ in all the cases.

ior, previously shown in a disk oscillator. These models captured many details of the steady state response of the physical system and hence can be used for a studying complicated networks of these device. A van der Pol-Duffing system (equation 3.1) shows limit cycle being entrained by forcing frequency when the forcing is close to the natural frequency of the system. Steady state response of the forced Mathieu-van der Pol equation (3.9) consists of either 2:1 subharmonic periodic motion or 1:1 periodic motion or quasiperiodic motion, depending on the forcing frequency and the forcing amplitudes, both parametric and nonparametric.

The hysteresis observed in numerical simulations with slowly varying forcing frequency (Figure 3.4 and 3.1) is explained by changes in the nature of the steady state due to bifurcations in the slow flow equilibria. For example, the jump upwards in Figure 3.4 is due to passage from region A to region B in the process of which a saddle-node bifurcation occurs and a stable periodic motion disappears.

The findings may be summarized briefly in words (for fixed α) by stating that parametric excitation is most important when ω is close to the unforced frequency of the oscillator (here taken as unity), or, in other words, when the detuning k_1 is close to zero, and when F is small. Nonparametric forcing takes over when $|k_1|$ is a little larger or when F is larger. Quasiperiodic behavior occurs when $|k_1|$ becomes sufficiently large for given F.

Chapter 4

Finite Element Techniques for Calculating Substrate Losses

A typical disc oscillator is attached in some way to a plate or block that is quite large and thick relative to the disc. As the disc oscillates it puts forces on the large substrate, resulting in the generation of stress waves in the block. These stress waves carry energy away from the oscillator, resulting in what is known as "geometric damping," energy lost to the oscillator due strictly to the geometry of the problem and the way in which stress waves propagate.

The conventional approach of analyzing the MEMS is to isolate it and look at the effect of different loading conditions. A fixed or free boundary condition is applied at its anchor. The analysis doesn't consider interaction of the MEMS with the substrate and hence the resulting losses due to the transmission of energy to the substrate are not considered. As will be shown later, these losses become very important when the size of the anchor is large or when the frequency is high. This work considers the the coupling of MEMS motion to the substrate.

The disc oscillator-substrate system is modeled using the finite element method. Owing to the large relative size of the substrate it is not possible to model the substrate in its entirety. Hence the domain of analysis using the finite elements needs to be truncated to a manageable size and the effect of wave propagation into the remaining substrate is approximated as the propagation into an infinite domain. Various methods have been used to approximate the infinite domains in previous works. A brief summary of these follow:

4.1 Theoretical Approach

Zhili et. al. [45] developed a theoretical approach to model the substrate and hence determine the losses in cantilevered beams and disc shaped resonators. The response of the resonant structure was determined from FEA or from analytical expressions, in case of beams. Fixed boundary condition is assumed at the anchor of the structure. The resulting stresses at the anchors drive the substrate, which is assumed to be an infinite elastic plate in case of cantilevered beams. The displacement field in the substrate is obtained analytically by modeling its behavior with Naiver's elastodynamic (NED) equation, subjected to the above boundary conditions. Work done by disk pressure is calculated by integrating the product of shear stress at the anchor with the displacement, over one cycle of forcing. This gives the loss from the system to the substrate per cycle. The ratio of total energy of the resonator to the energy lost per cycle, gives Q for the device.

This approach has limitations, that it assumes the wavelength of propagating waves to be much larger than the thickness of the vibrating structure and hence assumes the propagating waves to be 2D. It is also unable to capture the effects of wave reflections at discontinuities in the substrate, since the substrate motion doesn't drive the resonator .

4.2 Hifidelity MultiPhysics Simulations

In this approach, the resonator system is partitioned into modular subsystems consisting of the substrate, resonator and the electrostatic actuators. Each of these is modeled independently and then integrated by matching the interface conditions. Similar to [45], this approach assumes the substrate to be a semi-

infinite elastic medium. Motion of the substrate is assumed to be a superposition of various modes of wave propagation and the contribution of various modes of the substrate to a particular motion is obtained using a numerical scheme [46, 47].

The resonator response is calculated from FEA and a response matrix, relating the force and displacements at the anchor nodes, as well as the excitation nodes is constructed. Another response matrix is constructed by using an electromechanical model between the actuator nodes on the substrate and the corresponding excitation nodes on the resonant structure. Yet another response matrix relating force and displacements corresponding to points on the substrate is constructed. This assumes the substrate to be an infinite half space and the displacements corresponding to a given load are obtained by adding up contributions from different wave modes. Combining the three response matrices, a combined response matrix of the entire structure is constructed which is used to derive the stiffness and the damping matrices and hence calculate Q.

This approach has a disadvantage that a separate response matrix needs to be calculated for the substrate, every time the geometry for resonator anchor is changed. Also the calculation of response matrix for the substrate is computationally intensive. This method admits no discontinuities in the substrate hence the effect of substrate features like mesa structures explained in the next chapter cannot be included directly.

4.3 Truncated Domain FEA Approaches

These finite element based methods truncate the substrate at finite dimensions and apply various boundary conditions at the edge so as to approximate the effect of infinite domains.

4.3.1 Lossy Elements

This is the simplest method of applying infinite domain approximation. It involves placing viscous elements at the edge of the truncated domain. These elements have higher damping coefficient than the material of the truncated domain. The propagating waves are attenuated due to higher damping of these elements. However the main drawback with this approach is that a sudden change in the material impedance induces spurious reflections at the boundary. Other drawbacks are that they are effective only for the cases when the incoming wave is almost normal to the boundary. Also reflections are possible from the outer edge if the domain containing the lossy elements isn't large enough.

4.3.2 Perfectly Matched Layer

In this approach the infinite domain consists of elements which absorb all the energy of incoming waves without any spurious reflections and forms a Perfectly Matched Layer (PML). This approach was first used for electrodynamic simulations [48] and later extended to elastodynamics [49]. The elements in a PML use complex stretching of the coordinate axes to introduce damping to the waves. This is illustrated in the following case for a 1 D wave propagation which can be written as

$$\frac{\partial^2 u(x,t)}{\partial x^2} - \frac{1}{c^2}\frac{\partial^2 u(x,t)}{\partial t^2} = 0 \tag{4.1}$$

Assuming a solution of the form $u(x,t) = \hat{u}(x)e^{i\omega t}$ the following Helmholtz equation is obtained

$$\frac{d^2\hat{u}}{dx^2} + k^2 u = 0 \tag{4.2}$$

where $k^2 = \frac{\omega}{c}$ The solution is of the form

$$\hat{u}(x) = c_1 e^{i(kx)} + c_2 e^{-i(kx)}$$

In PML region the coordinate axes are stretched and the new coordinates are

$$\tilde{x} = \int_0^x \lambda(s) ds$$

$$\frac{d^2u}{d\tilde{x}^2} + k^2 u = 0 \tag{4.3}$$

which can be expanded to

$$\frac{1}{\lambda}\frac{d}{dx}(\frac{1}{\lambda}\frac{du}{dx}) + k^2 u = 0. \tag{4.4}$$

If $\lambda = 1 - i\sigma(s)/k$, where the choice of σ is discussed next, the solution to the above equation becomes:

$$u = c_1 \exp(-\int \sigma ds) \exp -ikx + c_2 \exp(\int \sigma ds) \exp ikx$$

If σ is chosen such that it is zero at the boundary the solution would be same for both media and hence the wave would enter the PML without any reflection at the boundary. The wave would attenuate if σ increases in magnitude away from the boundary. In a finite element formulation this transformation effectively leads to complex stiffness and mass matrices.

4.3.3 Infinite Elements

These elements provide a quiet boundary to the model by using special shape functions [50]. Regular shape functions are used to model the displacement variables while growing shape functions are used for position variables.

For example in a 1D case position can be written in terms of nodal variables as

Figure 4.1: The local position variables for the representative element in a 1D infinite element.

$$x = S_1 x_1 + S_2 x_2$$

The shape functions are

$$S_1 = \frac{2\xi}{1-\xi} \quad and \quad S_2 = \frac{1+\xi}{1-\xi}$$

This gives

$$x = x_1 \quad at \quad \xi = -1$$

$$x = x_2 \quad at \quad \xi = 0$$

and

$$x \to \infty \quad as \quad \xi \to 1$$

Hence the position coordinate approaches infinity at the farther edge of the element. The displacement on the other hand can be written as:

$$u = \frac{1}{2}\xi(\xi - 1)u_1 + (1 - \xi^2)u_2 \tag{4.5}$$

This goes to zero at ξ=1. Hence displacement of incoming wave decreases to zero as it approaches the farther edge of the infinite element, where x $\to \infty$. These

are provided as special purpose elements in ABAQUS for 2D, 3D and axisymmetric analysis. They are shown to work well for static, dynamic and perturbation analysis.

4.4 Modeling Substrate Losses for Dome Resonator

The modeling and analysis of substrate losses are performed on disc and dome shaped resonators. The techniques used here are easily and directly extendable to other geometries.

The dome resonator modeled here consist of a thin, buckled, circular plate with a hole in the center, anchored to the substrate at its periphery. It is made of polysilicon, which is an isotropic material. The typical diameter of these domes ranges from 10 μm to 40 μm. The experimental results presented in the next chapter correspond to a dome resonator of outer diameter 10 μm and inner diameter 2 μm and were measured for the second axisymmetric mode, corresponding to a frequency of 104 MHz. The mushroom shaped disc resonators which were discussed in the chapter 2 were also considered in simulations. These devices are fabricated on silicon on insulator wafers (SOI) and hence the substrate is layered, consisting of silicon, silicon dioxide and polysilicon on the top. A layered structure was considered in the simulations. A detailed discussion on the FEA follows.

The first simplification in the analysis is due to circular geometry of the resonator and hence only an axi-symmetric model is considered for analysis and design modifications are considered only on the axi symmetric modes of the oscillator. Although it cuts down on the ability to analyze each and every motion of the resonator, the positives, owing to fewer degrees of freedom in understanding the effect of a broad range of design parameters on the Q outweigh the limitations.

The axisymmetric analysis also gives some insight into the design for the non axi-symmetric cases.

Since the far field displacement in the half-space goes as $\sim 1/r$, this can be achieved by using the linear interpolation function for displacement in the elements. The infinite elements (CINAX4) work for the static as well as for the steady state dynamic analysis of the axisymmetric system.

The domain of analysis is shown in Figure 4.2 &4.3. The boundary of domain is circular as the best results with the infinite elements are obtained when the incoming wave is normal to the element edge. The nodes on the surface are spaced farther with the increasing distance from the resonator. The substrate is modeled with linear elements while the resonator is modeled with quadratic elements, as the primary resonant mode is bending and the stress varies quadratically along the thickness in that case. A tie surface constraint was applied between the resonator and substrate nodes, so as to avoid spurious reflections caused by free nodes of resonator. Material properties are considered isotropic, which is not the case for silicon but still is a good approximation. The infinite elements can't be applied from the GUI of ABAQUS or using a Python script, hence they need to be applied once the input file for the model is generated. The infinite elements need to be numbered in a specific order, different from an equivalent continuum element.

4.4.1 Calculation of Q using Energy Approach

In this approach Q is calculated from the basic definition where

$$Q = \frac{\text{Energy of the resonator}}{\text{Total loss per unit cycle}}$$

The energy terms in the above equation correspond to a steady state response of

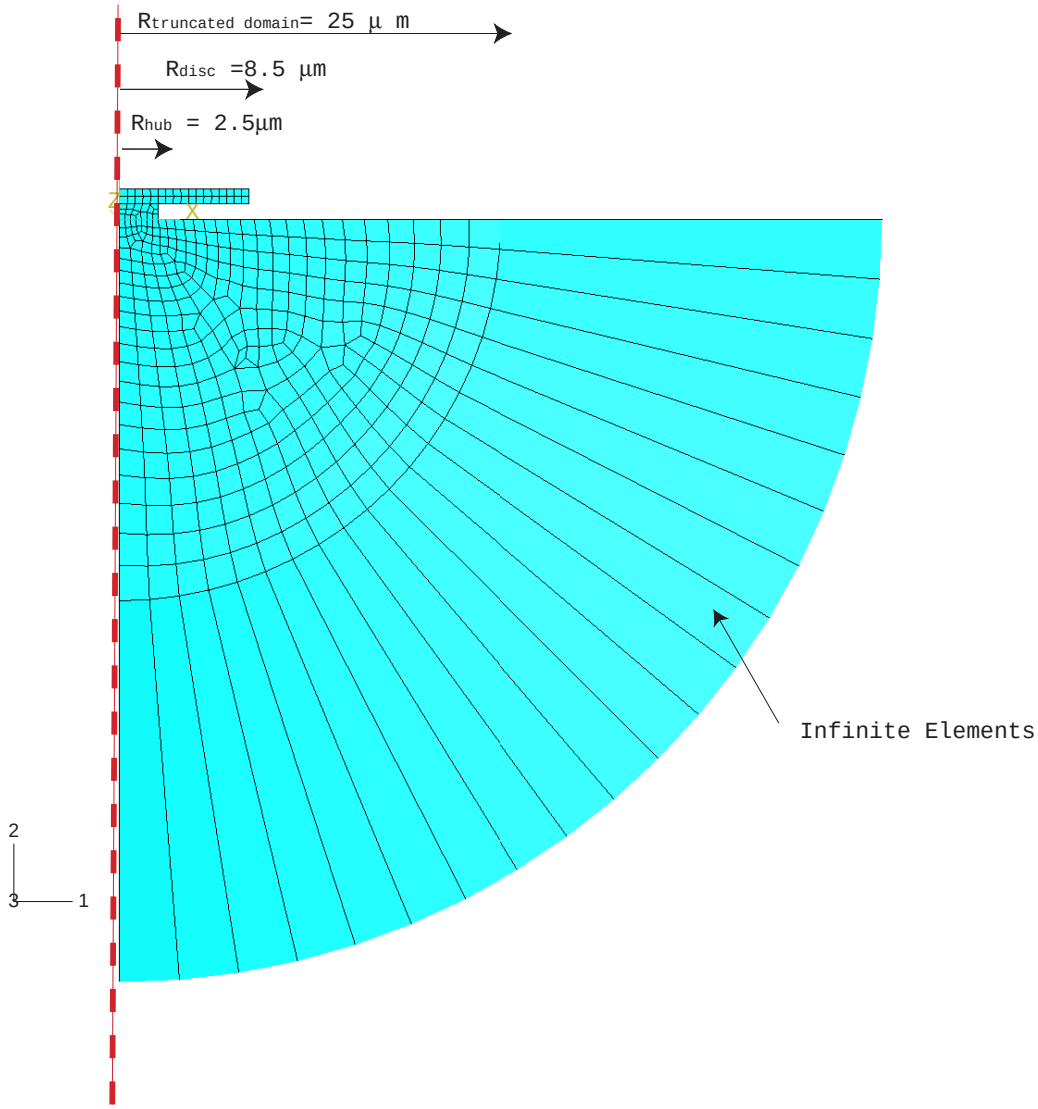

Figure 4.2: Finite element model for a disc of radius 8.5 μm, hub radius of 2.5μm. The substrate is truncated to a radius of 25 μm. CINAX4 axisymmetric infinite elements are stacked at the end.

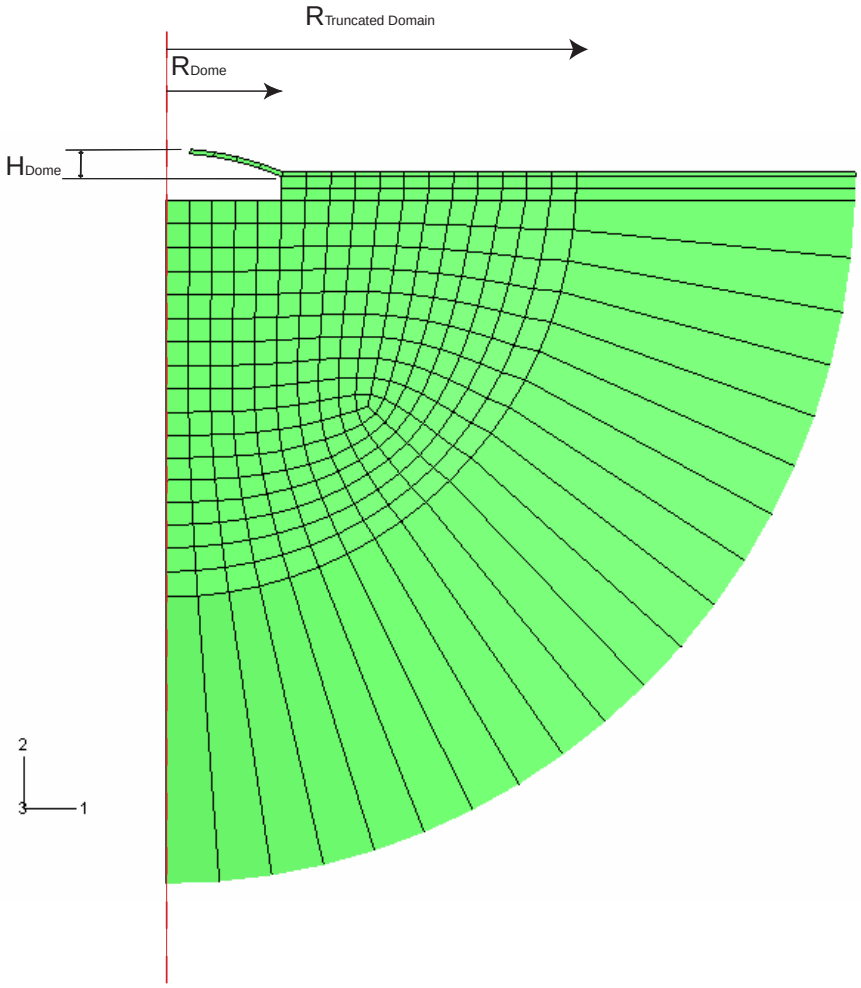

Figure 4.3: Finite element model for a dome of radius 5 μm, height of 0.5μm. The substrate is truncated to a radius of 18 μm. CINAX4 axisymmetric infinite elements are stacked at the end.

the resonator to a forcing close to the resonant frequency of the disc. Direct steady state analysis is a perturbation procedure, which gives the steady state response of the structure by performing a linear perturbation on the base state [50]. A modal analysis step precedes this step, to determine the frequency corresponding to the mode for which Q is sought. A predefined variable in Abaqus, ALLSE stores the value of total strain energy for the system, while the variable ALLQB gives the value of total energy stored in the quiet boundaries or the infinite elements. The ratio of two gives the Q for the device which is calculated in the user subroutine GETVRM. It is assumed in this analysis that all the energy lost by the resonator is stored in the infinite elements. Hence the truncated domain needs to be relatively small in this case. The converged value of Q for a disc shaped resonator of outer radius 5 μm and inner radius 2.5 μm at the first mode resonant frequency of 118MHz is 53.45. This method gives higher Q than the previous methods, because it assumes that energy lost from resonator is stored in the infinite elements. This is a good approximation for very small truncated boundaries. However the infinite elements give accurate results only if placed in the region where the stress gradients are not very high, hence the truncated domain needs to be of a reasonable size. This leads to significant amount of energy not being counted towards the loss as it is the part of the truncated domain and not of the infinite domain. Hence the denominator in the above expression which corresponds to total losses per unit cycle is reduced, leading to a higher Q. However it is seen that the Q value converges to above , with increasing size of the $R_{\text{Truncated domain}}$.

This is a very useful method to access the Q for a system with a large number of degrees of freedom as it involves performing a steady state analysis only at the resonant frequency. This method was also used to find Q for a full 3D problem

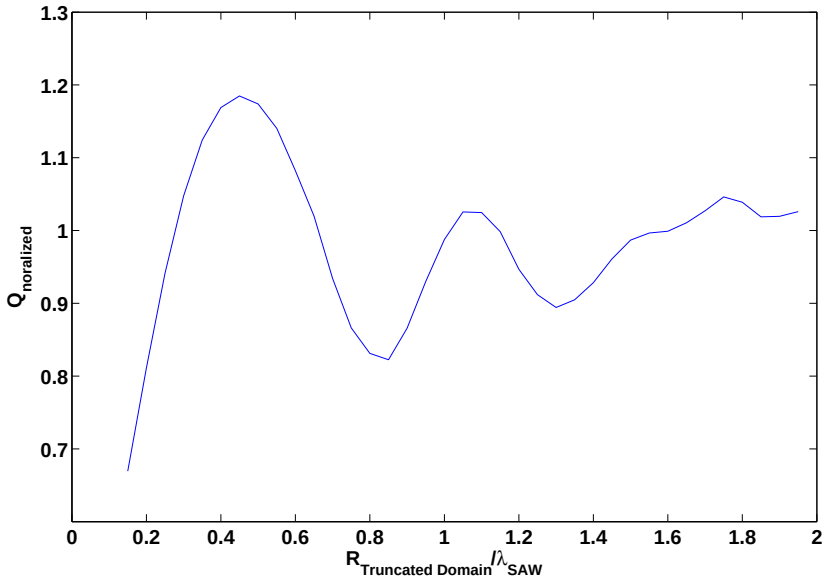

Figure 4.4: Variation of Q as a function of radius of truncated domain for the dome resonator, using the resonant response approach.

not discussed here.

Convergence Analysis

The effect of domain size on Q is shown in Figure 4.4. Hence we see that for $R/\lambda \geq 2$, the Q is constant with the size of the truncated domain. Mesh refinement doesn't have a significant effect on the Q.

4.4.2 Calculation of Q using Resonant Response Approach

This method calculates Q for the resonator in a way similar to the experiments. A steady state analysis is performed with a unit force to find the response of resonator substrate system close to first resonant mode. The quality factor is then defined as

$$Q = \frac{\omega_0}{\Delta\omega}$$

where ω_0 is the resonant frequency of the device and $\Delta\omega$ is the width of the amplitude frequency curve at the half power point as shown in Figure 1.1. This corresponds to an amplitude 3dB below the peak on a log plot of the response. The converged value of Q for a disk shaped resonator of outer radius 5 μm and inner radius 2.5 μm at the first mode resonant frequency of 118MHz is 45.56.

4.4.3 Calculation of Q using Resonant Amplitude Decay

The quality factor of resonator can also be obtained from the decay of the system amplitude from a steady state vibration condition. Transient dynamic analysis is performed for the system under periodic forcing close to the resonant frequency, leading to steady state modal vibrations. The forcing is then switched off and the system allowed to vibrate freely. An exponential curve is fit to the amplitudes of the resulting decaying temporal response. This can be used to determine the damping coefficient for the system and hence the Q.

$$Q = \frac{2\mathrm{m}\omega_0}{C}$$

.

where m is the mass of the resonator, ω_0 the resonant frequency and C the damping coefficient. The converged value of Q for a disc oscillator of outer radius 5 μm and inner radius 2.5 μm at the first mode resonant frequency of 118MHz is 45.23. This is the most time consuming method of those described here. The typical time needed for simulation is orders of magnitude higher than previously

described methods. However, the analysis is invaluable for verifying the results of various methods.

4.4.4 Calculation of Q using PML in HiQ Lab

In this method PML is used to model the infinite boundaries, resulting in system of equations with complex stiffness and mass matrices. Complex eigenvalues are obtained for the system of equations and the Q can be obtained as [51]

$$Q = \frac{\mathrm{Re}(\omega)}{\mathrm{Im}(\omega)}.$$

Unfortunately this technique was not directly amenable to ABAQUS at the moment. Hence HiQLAB [52] an FEA software designed specifically for simulating PML was used for calculation of the Q. The converged value of Q for a mushroom shaped resonator of outer radius 5 μm and inner radius 2.5 μm at the first mode resonant frequency of 118MHz is 37.68.

4.5 Parametric Study

A parametric study is performed to find the effect of various design parameters on the substrate losses.

Figure 4.5 shows the variation of Q as a function of the resonant frequency of the device. It is seen that the losses due to anchor coupling are higher for higher frequencies and the variation is almost exponential. Figure 4.6 shows the variation of Q as a function of the hub radius with the frequency of the resonator constant at 120MHz. The Q decreases with increasing hub radius. Increase in anchor loss with center frequency was reported by Wong et al. [18] in their designs.

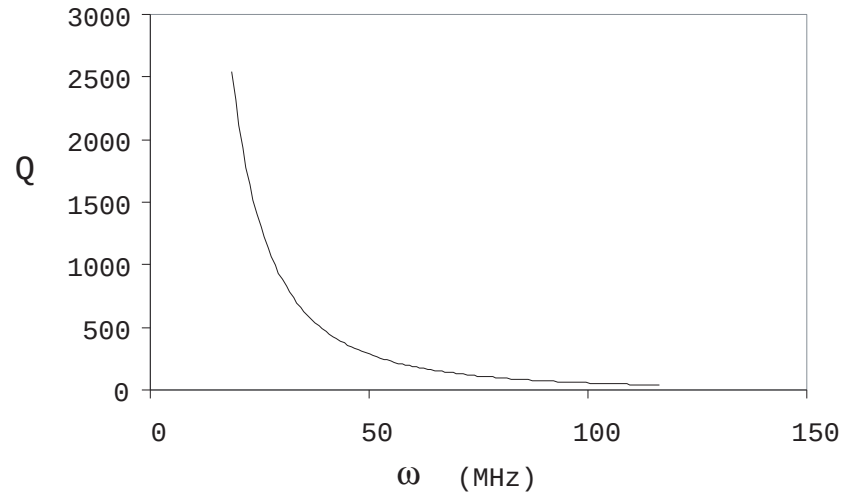

Figure 4.5: Variation of Q as a function of frequency of the oscillator, keeping the anchor radius constant. The resonant frequency was varied by changing the outer diameter of the disc oscillator.

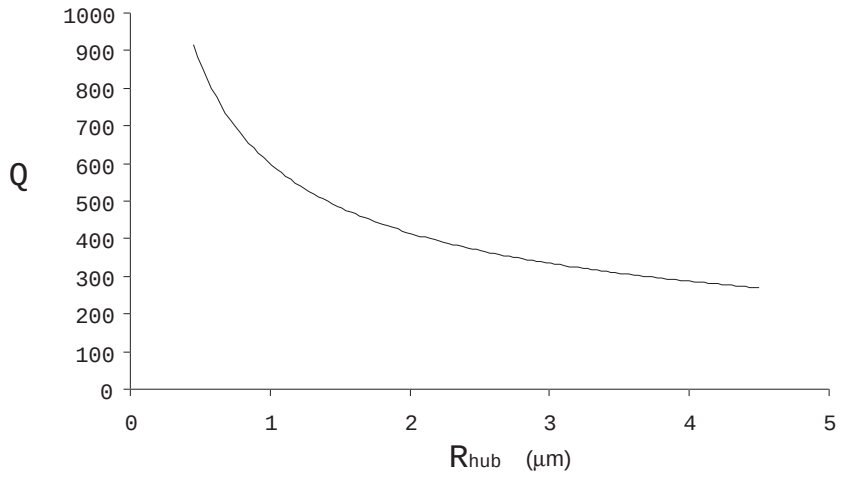

Figure 4.6: Variation of Q as a function of MESA depth for a disc oscillator of resonant frequency 1.13 GHz in the second radial mode.

4.6 Material Parameter Determination

The diameter and thickness of the dome resonator was directly measured from the SEM images. However dome height associated with out of plane curvature of the disc shaped structure could not be measured directly. An assumed value of dome height and the documented value of material properties were used to fit the modal frequencies obtained from the experiments. However it was not possible to fit the resonant frequency spread of the experimental data by just varying the dome height in the FEA. Due to in situ deposition of polysilicon during the fabrication process, to be described in detail in chapter 5, it is possible that some of the material properties may not be the same as the standard data for polysilicon.

Hence an optimization scheme shown in Figure 4.7 was used to best fit the frequency spectrum by simultaneously varying the material parameters and the dome height. The process required generation of new geometries for the values corresponding to better fit to the frequency spectrum. Hence a Python script was used to generate new geometries and perform modal analysis in Abaqus with Matlab performing optimization and giving a new value for material parameters and the dome height as input to the Python script. This process was used to fit the frequency spectrum of first four modes and was verified using first five. The properties hence obtained are the following.

Dome Height = 153 nm

Young's Modulus = 130 GPa

Density = 3300 kg/m^3

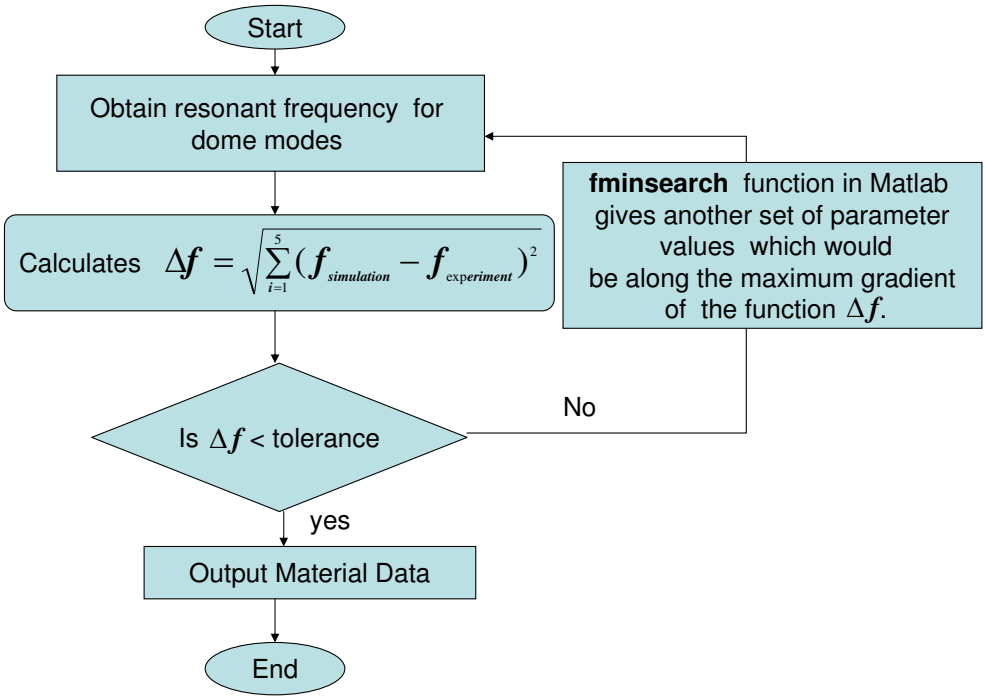

Figure 4.7: Scheme for determining unknown dome properties.

Chapter 5

Mesa Structure To Reduce Anchor Loss

Consider a MEMS resonator attached to substrate that is very large compared to the size of the resonator. As the resonant device vibrates it will lose energy to the substrate via the anchor, causing disturbances in the substrate that propagate away from the resonator in the form of stress waves. The stress waves consist of bulk acoustic waves (BAW) and surface acoustic waves (SAW) as shown in Figure 5.1. A large portion of the wave energy is in the SAW, which as suggested by the name, is confined close to the surface of the substrate. Analysis of a harmonic resonator on an infinite half space shows that 67% of the energy propagates in the form of SAW, 26% in the form of shear waves and 7% as pressure wave [53]. This energy is soon scattered or dissipated into the relatively infinite expanse of the substrate. Hence if this energy could be reflected back to the resonator, a significant improvement in device performance should be expected.

5.1 MESA Structure

Mesa structure consists of a trench (as seen in Figure 5.2) which surrounds the dome oscillator and is able to reflect the emanating SAW back towards the oscillator hence improving the Q. Viktorov [4] showed in his work on SAW hitting a corner, that depending on the angle of corner, a portion of the incoming wave energy reflects, the remaining either transmits as a SAW or propagates into the bulk in the form of BAW as shown in Figure 5.3. The amount of energy reflected depends on the angle subtended by the corner. It was shown that the maximum reflection occurs for an corner angle of 60^0. Such a design was not feasible with

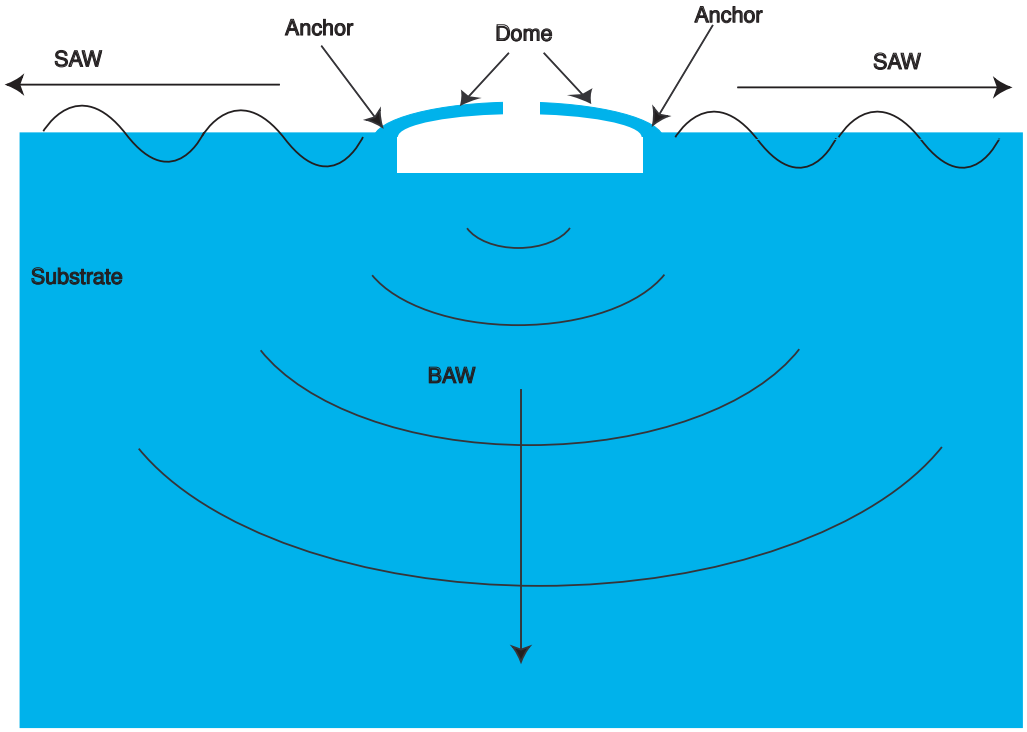

Figure 5.1: Anchor coupling of dome resonator with substrate.

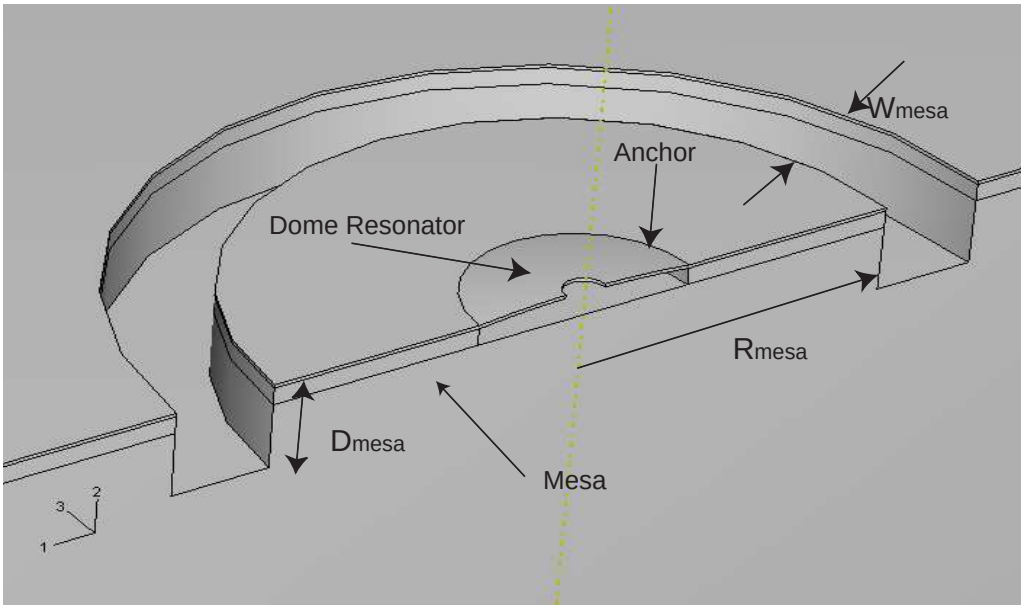

Figure 5.2: Mesa surrounding a dome resonator.

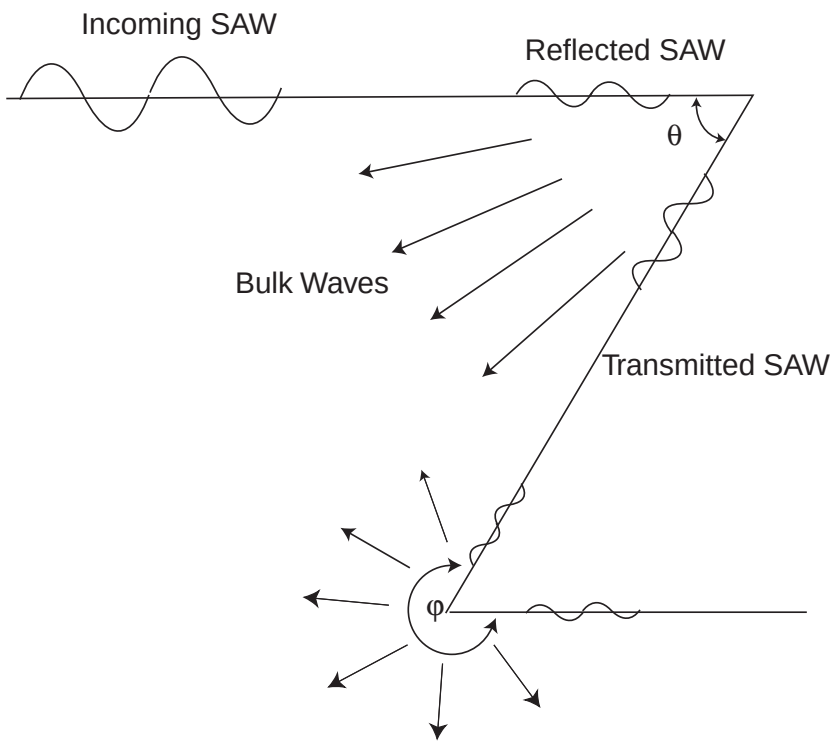

Figure 5.3: Effect of a corner on a propagating SAW as shown by Viktorov [4]. Here the effect of corners at the top and the bottom of a mesa like structure are shown.

the available lithographic techniques, however significant reflection ($\sim 65\%$) is seen even in the case of a 90^0 corner.

A finite element plot of the effect of mesa on the incoming waves is shown in Figure 5.4. It is seen that the wave splits at the corner, primarily in two directions. It is partly reflected and partly refracted in the perpendicular direction. A small fraction is also seen to propagate into the substrate as BAW. As can be seen from the pictures, a good portion of the outgoing wave is reflected back by the mesa.

For correct dimensions of mesa, the reflected wave interferes constructively with the outgoing wave and as a result forms a standing wave pattern, which traps energy inside the mesa and is shown to improve Q by up to four times. The SAW

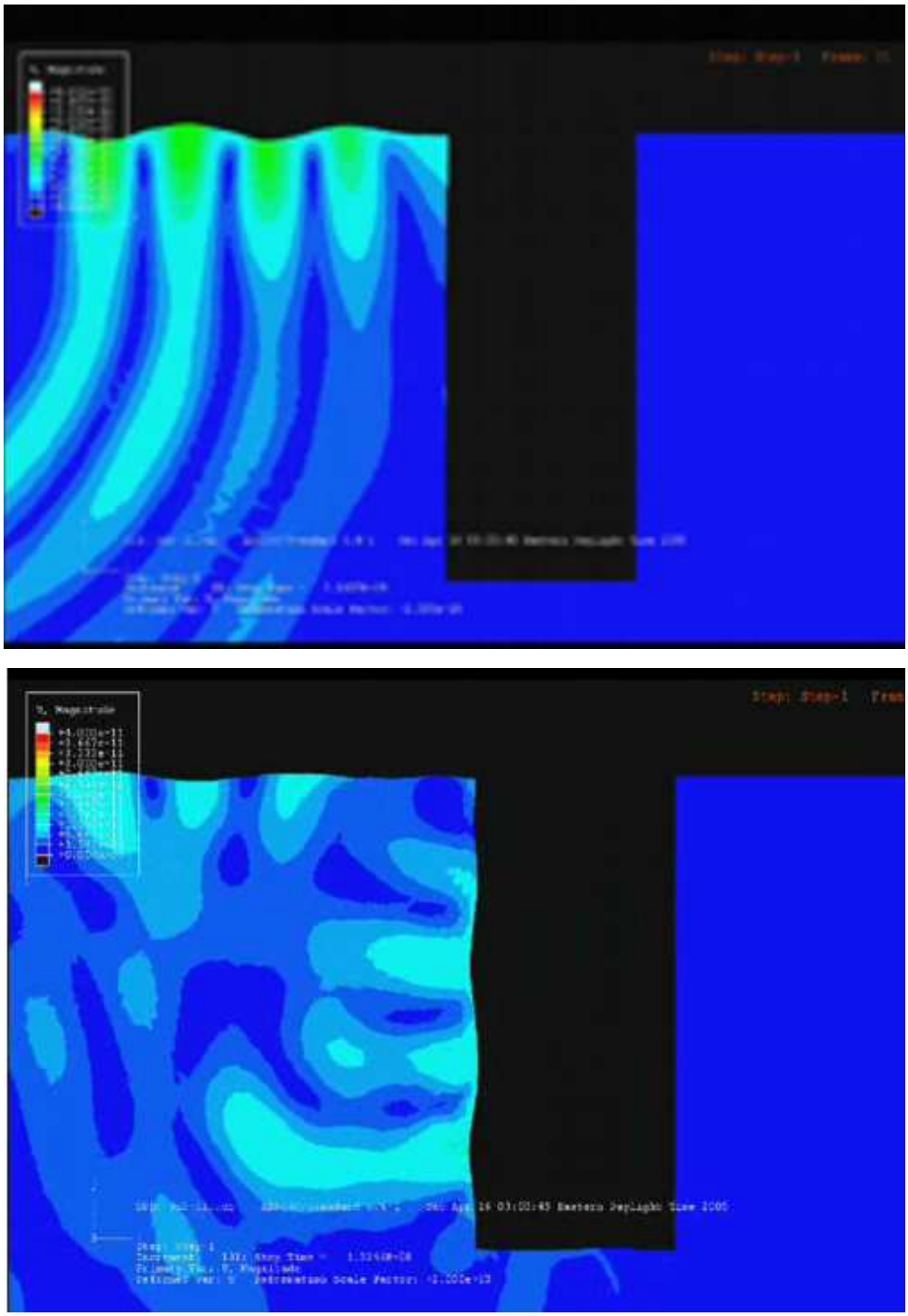

Figure 5.4: Effect of mesa on incoming wave. a)Before reflection. b)After reflection.

energy is reflected at corners and hence the reflection occurs at both the top and the bottom of the mesa. The transmitted SAW at the top edge of the mesa is partially reflected and partially transmitted at the bottom edge but is mostly propagated into the bulk owing to the angle of the corner ($> 180^0$). A portion of these waves arising from the bottom of the mesa interfere with the resonator motion leading to the dependence of Q on the depth of the mesa. This essentially forms a feedback mechanism which applies a force to the resonator, with a delay corresponding to the time of travel for the SAW. The control in quality factor using a feedback back mechanism has been earlier used to enhance mapping of DNA-protein complexes using dynamic scanning force microscopy (SFM) [54], high speed tapping mode imaging [55] and in chemical and biosensor [56].

Although the idea of having a trench around buildings and heavy machinery has been used for vibration isolation [57], [58] i.e. to isolate the building from outside disturbances, this is the first instance of using this design for trapping energy, hence improving quality of a micro oscillator. Traditionally trenches filled with oxide have also been used in transistor fabrication to provide electrical isolation.

Next a qualitative analysis of the effect of the delayed feedback on the effective Q is given.

5.1.1 Simplified Model

The outgoing wave amplitude is directly related to the amplitude of motion of a representative point on the oscillator. Hence a simplified model of the system is:

$$m\ddot{x}(t) + c\dot{x}(t) + kx(t) = F_0 \sin \omega t + Ge^{i\phi}x(t) \tag{5.1}$$

where x(t) is the displacement of a point on the disk, m is the effective mass, c the damping and k the stiffness for the system, G is the gain for the feedback and

ϕ is the phase difference introduced by the delay and depends on the size of the mesa here.

The identities

$$e^{i\phi} = \cos\phi + i\sin\phi$$

and

$$ix(t) = \frac{\dot{x}(t)}{\omega}$$

could be used to rewrite equation 5.1 as

$$m\ddot{x}(t) + c_{\text{effective}}\dot{x}(t) + k_{\text{effective}}x(t) = F_0\sin\omega t \tag{5.2}$$

where

$$c_{\text{effective}} = (c - \frac{G\sin\phi}{\omega})$$

$$k_{\text{effective}} = (k - G\cos\phi)$$

Hence

$$Q_{\text{effective}} = \frac{2m\omega_{\text{effective}}}{c_{\text{effective}}} \tag{5.3}$$

$$= Q_0\frac{\sqrt{1-\frac{G\cos\phi}{k}}}{1-\frac{G\sin\phi}{c\omega}} \tag{5.4}$$

is a function of ϕ. As will be shown later, ϕ varies with the radius of the mesa.

For the dome resonator,

$$m \sim 4\pi r^2\rho_{\text{silicon}} \sim 1.76\text{x}10^{-7}\text{kg}$$

$$c = \frac{2m\omega_0}{Q_0} \sim 0.052\frac{\text{kgm}}{s}$$

$$k = m\omega_0^2 \sim 1.8\text{x}10^{-9}\frac{\text{N}}{\text{m}}.$$

Using asymptotic expansion the expression can be written as:

$$Q = Q_0(1 - \frac{G}{2k}\cos\phi + \frac{G}{c\omega_0}\sin\phi + \text{h.o.t.}) \tag{5.5}$$

solving for $\frac{dQ}{d\phi} = 0$ following condition is obtained for stationary points,

$$\begin{aligned} \tan\phi \quad &\sim -\frac{2k}{c\omega_0} = -\frac{2m\omega_0^2}{c\omega_0} = -Q_0 \\ &\sim -700 \qquad (5.6) \\ \phi \quad &\sim \frac{n\pi}{2} \qquad (5.7) \\ \frac{d^2Q}{d\phi^2} \quad &= \frac{G\cos\phi}{2k} - \frac{G\sin\phi}{c\omega} \qquad (5.8) \end{aligned}$$

Q has maxima for

$$\phi = \frac{(4n+1)\pi}{2} \text{ where n} = 0, 1, 2..... \tag{5.9}$$

and a minima for

$$\phi = \frac{(4n+3)\pi}{2} \text{ where n} = 0, 1, 2..... \tag{5.10}$$

For traveling wave the phase at position x is given by kx, where $k = \frac{2\pi}{\lambda}$ is the wave number. Hence phase shift introduced by the wave traveling to the edge of the mesa and back is,

$\phi = k(2R_{\text{mesa}}) = \frac{4\pi R_{\text{mesa}}}{\lambda_{\text{SAW}}}$,

an increase in Q is expected for $R_{\text{mesa}} = \frac{\lambda_{\text{SAW}}}{8}, \frac{5\lambda_{\text{SAW}}}{8}, \frac{9\lambda_{\text{SAW}}}{8}...$

while a decrease is expected for $R_{\text{mesa}} = \frac{3\lambda_{\text{SAW}}}{8}, \frac{7\lambda_{\text{SAW}}}{8}, \frac{11\lambda_{\text{SAW}}}{8}...$

5.2 Experiments

To verify the FEM simulations, experiments were performed on a dome shaped membrane resonator as shown in figure 5.5 and previously described in [59], [60]. This particular resonator geometry was selected because of its ease of fabrication

and testing as well its ability to reach high frequencies where the effect of mesa isolation will be more pronounced.

5.2.1 Fabrication

To form the dome resonator a 1.53 μm thick sacrificial layer of SiO_2, followed by a 200 nm thick LPCVD polysilicon film is deposited on a silicon substrate. A single layer of photolithography followed by a CF4 RIE etch patterns 2 x 2 μm etch holes into the device layer. The etch holes permit a subsequent dip in hydrofluoric acid (HF) to undercut the polysilicon device layer and create a suspended membrane. The time of the wet etch determines the radius of the suspended membrane. In this case a 3-minute 49% HF bath produced resonators with a 10.72 μm diameter. Shallow curvature in the membrane is created by allowing polysilicon film stress to be relieved through out of plain projection. Curvature in the membrane serves to both increase the resonant frequency as well as enable thermal actuation. The rigidity of the dome resonators also permits a second layer of photolithography to be performed, which defines the outline of the area that will be removed to create the MESA structure. Using Shipley 1813 resist as a mask, a short RIE silicon etch followed by an ICP oxide etch is used to penetrate the device and oxide layer. A subsequent ICP DRIE silicon etch penetrates approximately 13 μm into the silicon substrate wafer to form the isolation MESA out of the unetched portion of the wafer (Figure 5.5).

5.2.2 Testing

Dome resonators from the same fabrication sequence, both with and without the MESA were loaded into a custom vacuum chamber. The MEMS chip is placed

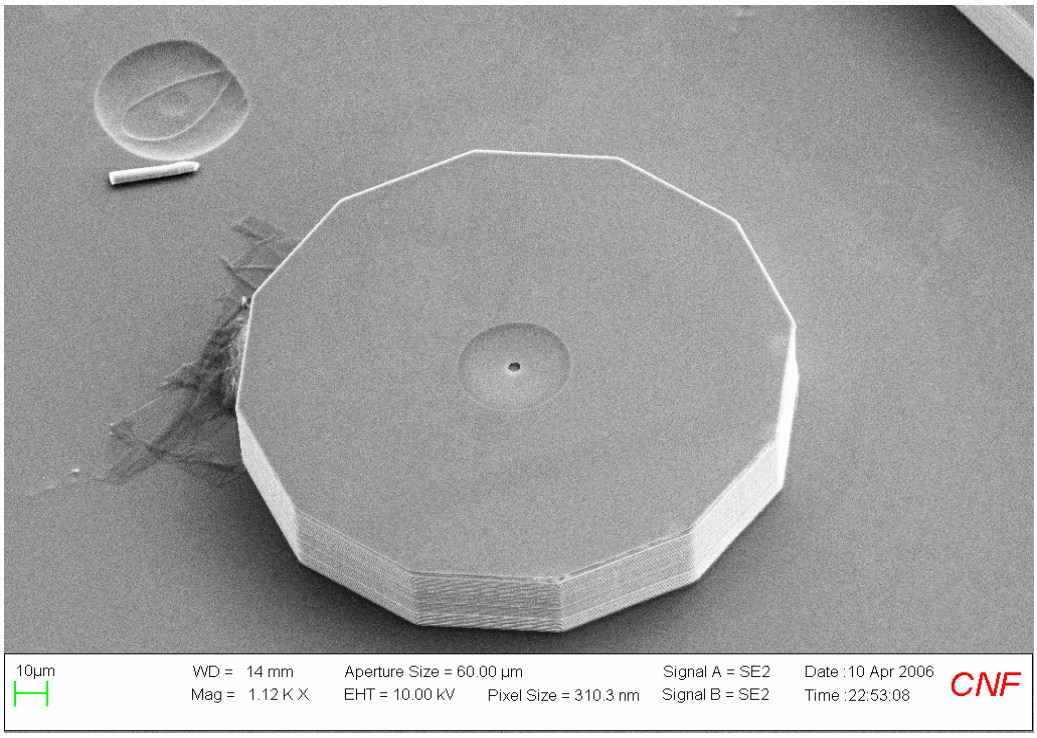

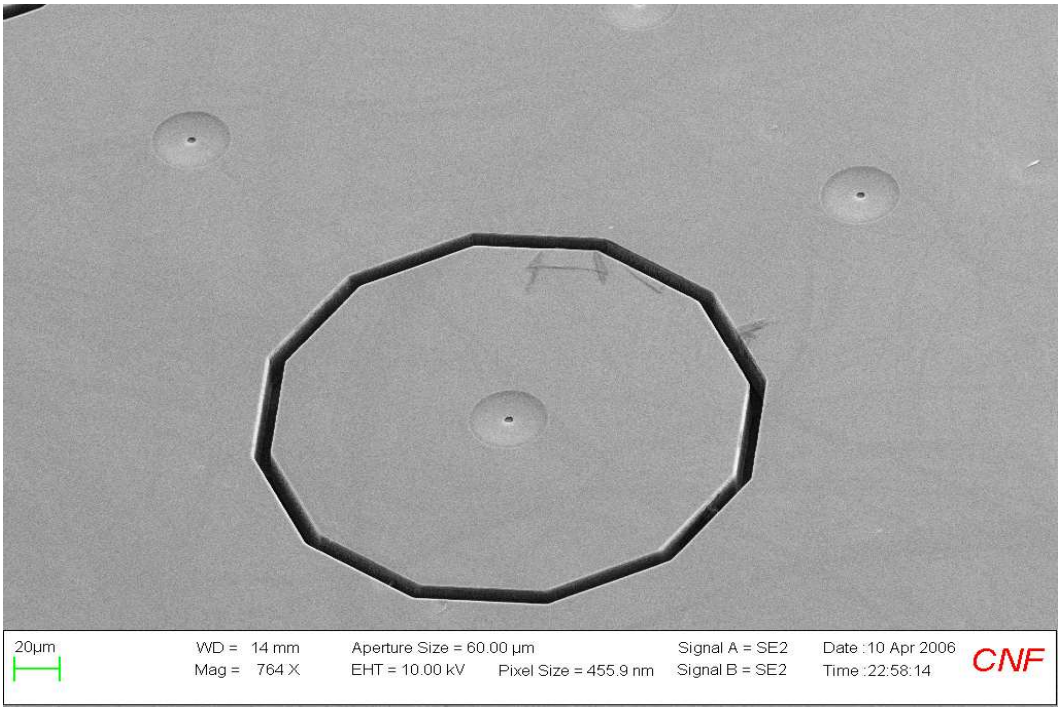

Figure 5.5: SEM image of domes with mesa. a) Mesa structure of infinite width. b)Mesa structure of finite width.

in a vacuum chamber capable of being pumped to pressures below 1 mTorr, low enough that dissipation due to surrounding gases is insignificant. Optical excitation and detection, previously described in [61], were used to stimulate and measure resonant vibrations in the dome membrane. An overview of the experimental setup is shown in Figure 5.6. The samples are placed near a quartz window in the vacuum chamber. A long working distance, 0.35 NA, 20x microscope objective is placed outside the vacuum chamber. Light from a HeNe laser (λ=633 nm) and an argon ion laser (λ= 2μ m) is directed through the microscope objective and focused to a 2μ m diameter spot on the surface of the wafer. Heat dissipated by the diode laser into the polysilicon film is used to induce displacement in the MEMS structure. Local changes in temperature produced from the focused diode laser produce stress gradients in the membrane, which are relieved through out-of-plane displacement. When the intensity of the diode laser is modulated at a resonant frequency of the membrane, the periodic relaxing and expanding can excite standing wave patterns in the resonator [62].

The incident light from the HeNe laser is partly transmitted through the thin polysilicon film. The transmitted component reflects from the substrate back through the poly membrane, interfering with the directly reflected light, forming a Fabry-Perot cavity interferometer. When the resonator experiences out of plain deformation, the amplitude of the net reflected light becomes directly proportional to the amplitude of displacement within the laser focal volume [60]. The location of the laser spot is optimized to achieve the highest amplitude reflected signal, which is directed into an AC-coupled photodetector. The photodetector output is measured by a spectrum analyzer (also used to drive the modulated diode laser), which records the amplitude and frequency of the mechanical MEMS motion. A

typical spectrum for the dome oscillators will be composed of a multiple resonant modes ranging from γ_0 axisymmetric modes, to γ_1 non-axisymmetric modes.

To determine the baseline Q-value for the resonators in the fabrication sequence, a set of domes with a continuous polysilicon layer (lacking the mesa feature) were first measured. In Figure 5.7 the black lines indicate the variance of the quality factors across the chip for a 104 MHz axisymmetric mode. On a separate die, (immediately adjacent to the previously mentioned die) multiple diameter mesas, each with their own dome resonator located at the center of the mesa, were tested. By varying the radius of the mesa, for a given mode of oscillation and thus constant SAW wavelength, varying interference patterns were seen for different mesa dimensions (Figure 5.7). For example, in mesas with a radius close to 0.75 λ (which were predicted to have constructive interference patterns), clear improvements were seen in the resonator Q value, suggesting that interference patterns were successfully coupling acoustic energy back into the mechanical motion. However, in structures with a mesa radius of λ, degradation in the Q-value over the non-mesa chip was observed, which could be attributed to an oscillating interference pattern which is out-of-phase with the micromechanical resonant motion. As the mesa diameter is increased, a clear oscillatory pattern with a period of 0.5 λ can be seen, supporting the conclusion that acoustic energy, ordinarily lost to acoustic wave propagation, can be successfully trapped within the mesa structure and, depending on the dimension of the mesa structure, can couple back to the resonator in either a beneficial or harmful way.

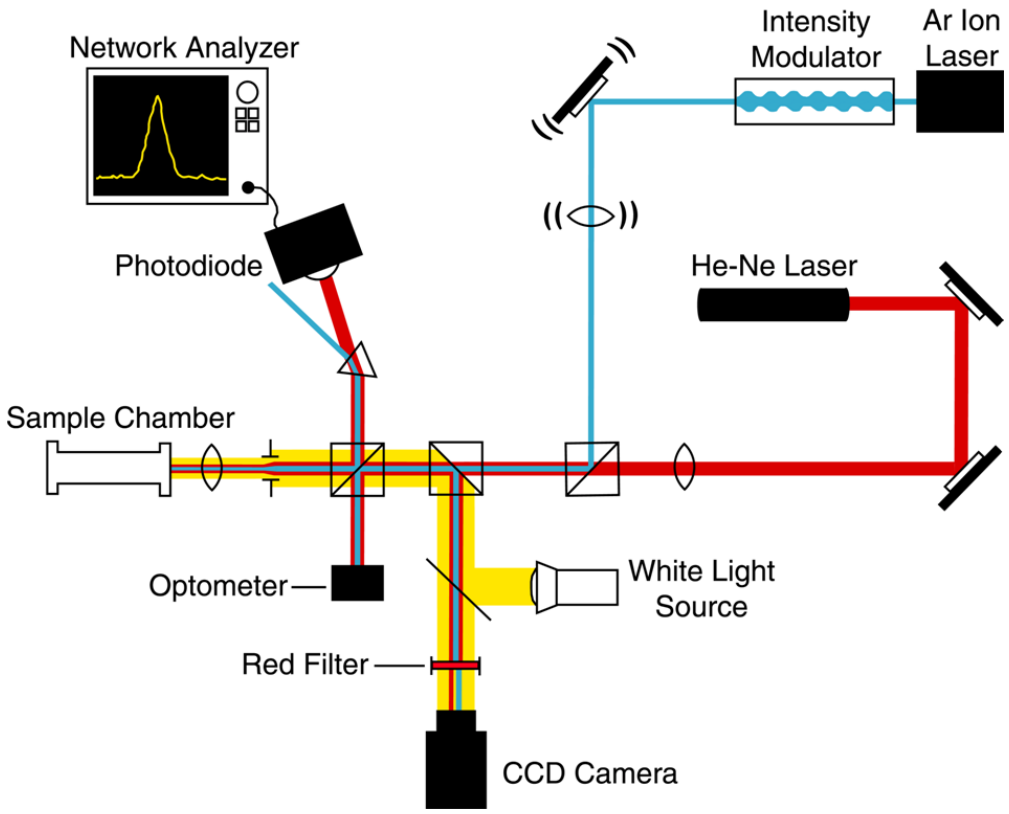

Figure 5.6: Experimental setup.

5.3 Numerical Results

Finite element simulations were performed with method described in chapter 4 using infinite elements. A parametric study of the dependence of Q is performed on the dimensions of the MESA structure.

5.3.1 Parametric Study with Mesa

Figure 5.7 shows the measured and computed variation of Q with radius of MESA for a 104 MHz flexural mode dome resonator for different mesa radii. Three measurements were performed on two sets of resonators, for each point on the graph. The depth of the mesa is 13 μm, while the width of mesa is infinite in the simulations. At this resonant frequency, the wavelength of SAW (λ_{SAW}) in Silicon is is 46.5 μm. It is seen that Q increases due to the mesa when R_{mesa} is close to 0.25λ, .75λ, 1.25λ, 1.75λ ... while there is a decrease in Q when R_{mesa} is .5λ, λ, 1.5λ, 2λ ... . This is expected if we consider the interference between the outgoing and incoming wave. Constructive interference in the first case adds energy to the system at resonance and hence increases the Q while destructive interference occurs in the second set which distributes energy to non-resonant modes. It is seen that the maximum increase in Q is with mesa radius of 1.75λ (Q =3400) while a prominent decrease is seen at a mesa radius of 0.5λ (Q=520), which can be attributed to the fact that the diameter of mesa at this frequency corresponds to λ_{SAW} and the mesa itself resonates at this frequency of excitation hence loosing much more energy to the substrate. This pattern is seen with oscillators of varying sizes and frequency.

The experimental data is plotted in the same plot and is shown by the dots. It not only shows an improvement in the Q of the devices but also shows the

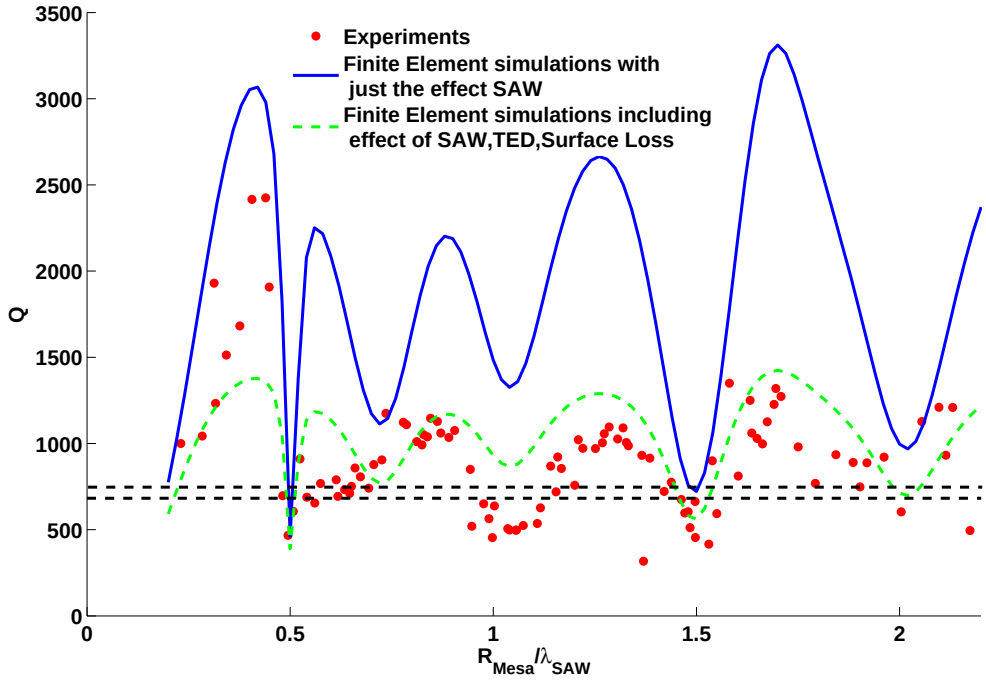

Figure 5.7: Variation of Q as a function of mesa radius for a dome oscillator of resonant frequency 104 MHz in second axi-symmetric flexural mode for an infinite width mesa of a depth of 13 μm. The two black lines show the maximum measured variation in Q, without mesa.

same pattern shown by the simulations. Up to 4X increase of Q is seen in these devices where the Q for this mode without mesa was 690. The improvement in Q predicted by the simulation is higher than the experiments. The additional losses can be attributed to the factors such as thermo elastic dissipation (TED), surface losses and material damping, which haven't been considered in the simulations.

It must be pointed out here that the frequency of variation of the crests and troughs of the Q vs. R_{mesa} was correctly predicted by the simple feedback model for the system in section 5.1.1. However the positions of troughs and crests was shifted by $\frac{\lambda_{\text{SAW}}}{8}$, which cannot be explained at present.

Modeling other losses

The thermoelastic damping (TED) is caused by irreversible heat flow across the thickness of the cantilever as it oscillates. The expression for TED for cantilevered beams predicted by Zener [63] is given by Houston and Photiadis [64] as:

$$Q_{\mathrm{TED}} = \frac{\alpha^2 T E}{c} \frac{\omega\tau}{1+\omega^2\tau^2}$$

E the Young's Modulus, α the thermal expansion coefficient, c the specific heat capacity, T the temperature, ω the resonant frequency and τ is the thermal relaxation time given as

$$\tau = \frac{a^2}{\pi^2\kappa}$$

a being the sample thickness and κ the thermal diffusivity. For the dome resonator Q_{TED} is 32440. Hence the dissipation through this mechanism is negligible for the given resonator.

The surface dissipation is given for a thin cantilevered beam is [64]

$$Q_{\mathrm{surface}} = \frac{bh}{2\delta(3b+h)} \frac{E}{E_l}$$

where δ is the surface layer thickness, assumed to be 20 nm to get a good fit of overall Q with the experiment. E_l is the loss modulus, typically assumed to be $\frac{1}{1000}E$ for materials away from glass transition temperatures. For the dome resonator, Q_{surface} is calculated as 1650 by assuming the dome to be a cantilevered beam of same area.

Similar pattern in Q vs R_{mesa} was obtained for the case of a disc shaped resonator fixed at the center as shown in Figure 5.8. This shows the robustness of using mesa for different kinds of structures.

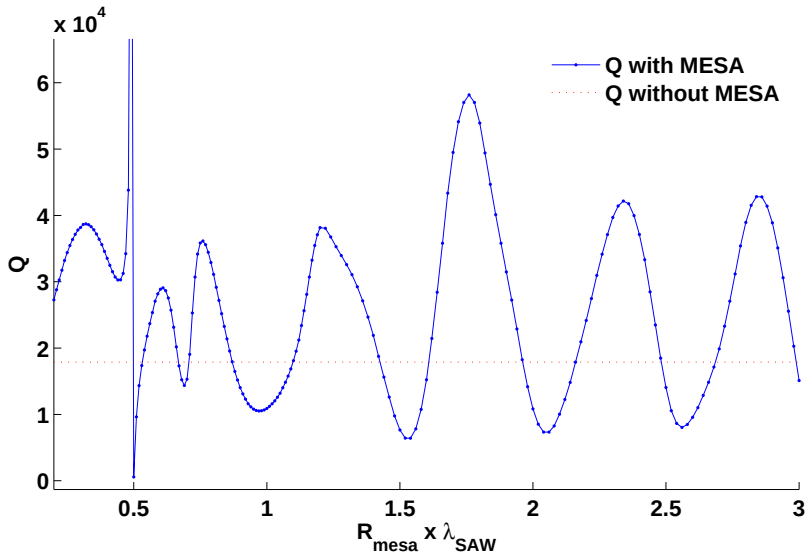

Figure 5.8: Variation of Q from FEM simulation as a function of mesa radius for a disc resonator similar to the one shown in Figure 1.2 at 1.3 GHz for second radial/breathing mode i.e. the mode in which the disk expands radially, uniformly in the circumferential direction.

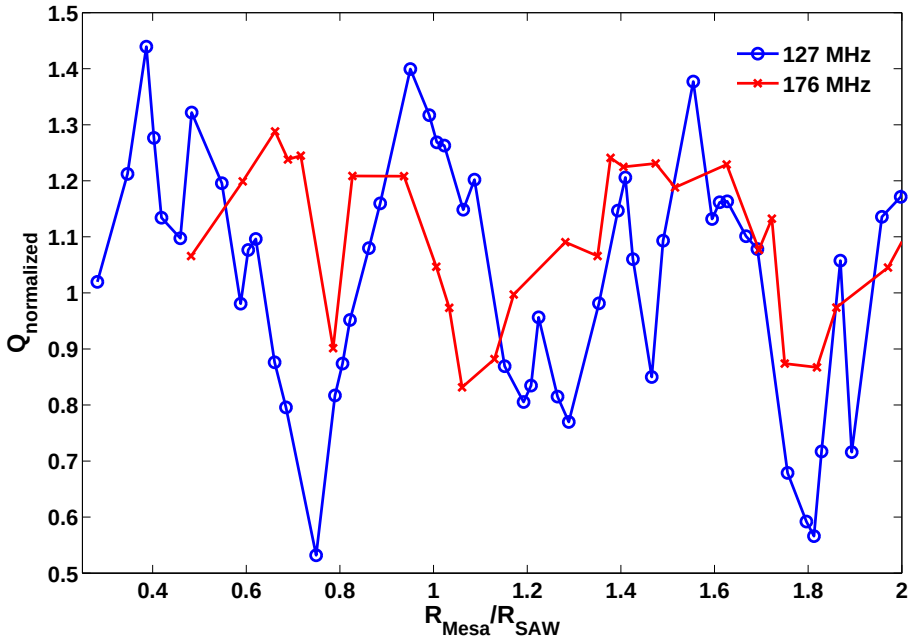

Figure 5.9: Experimentally observed Q for two non axisymmetric dome modes.

Non-axisymmetric Modes

Experimental results for two other modes of the dome are shown in Figure 5.9. It is seen that the 175 MHz mode shows similar variation as the 104 MHz mode but the 126 MHz modes shows just the opposite trend. These results are for non axi-symmetric modes and hence are not expected to match the simulations. Due to non axisymmetry of the modes, dissipation due to SAW is less compared to the axisymmetric modes and the losses corresponding to the anchor coupling are close to the surface loss. Hence the improvement in Q by using mesa is less than what is seen in the axisymmetric case.

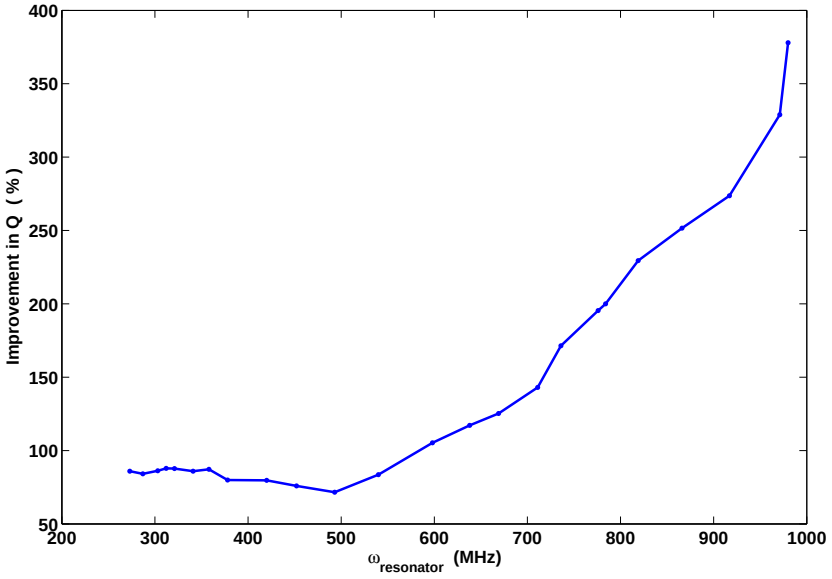

Figure 5.10: Percentage variation of Q as a function of oscillator frequency for a mesa radius of $1.25 \times \lambda_{SAW}$. The results are given for second radial mode of the oscillator.

Variation of Q with mesa frequency

Figure 5.10 shows the variation in improvement of Q for radial mode of disc oscillator of same hub radius but different frequencies. The results have been plotted for % change in Q with the introduction of a mesa. The depth and the width of the mesa remains constant It is observed that the gains in Q are very impressive for the higher frequency oscillators (GHz range) and the growth seems almost exponential. This can be attributed to the fact that anchor losses in the oscillators also increase exponentially. Since the mesa only traps the energy corresponding to the wave propagation, the same trend is seen in Q improvement. Another advantage of using mesas in the higher frequency case is that a smaller sized mesa can be used.

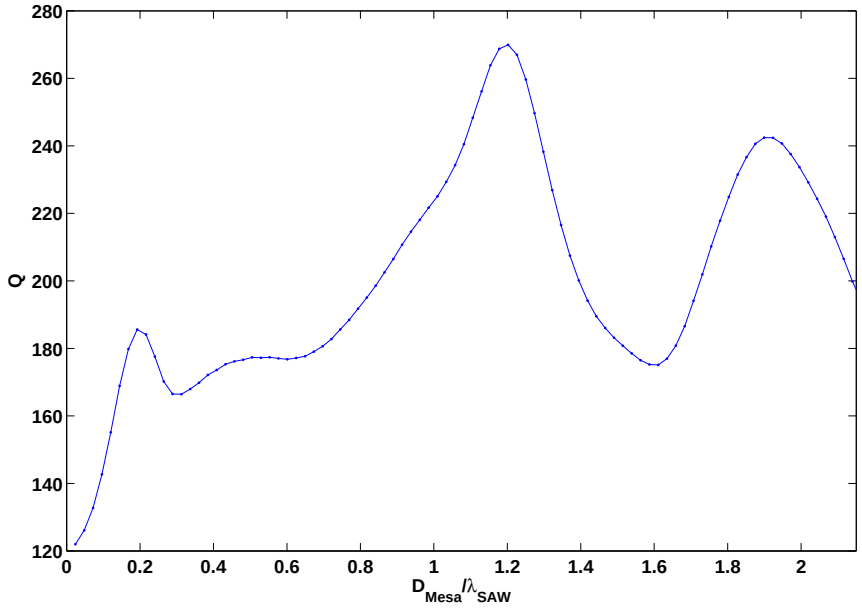

Figure 5.11: Variation of Q as a function of mesa depth for a disc oscillator of resonant frequency 1.13 GHz in the second radial mode. The mesa radius is kept constant at $1.25 \times \lambda_{\mathrm{SAW}}$.

Variation of Q with mesa depth

The effect of changing mesa depth on Q is shown next in Figure 5.11. The variation of the Q with mesa depth is also periodic with the frequency of the SAW wave. The surface wave transmitted at the mesa boundary travels to the bottom of the mesa and is reflected by the discontinuity at the bottom of the trench. The body waves generated by this discontinuity interfere with the incoming waves near the resonator either constructively or destructively. Similar variation in reflected signal with increasing depth of a vertical slit was predicted by Viktorov [4].

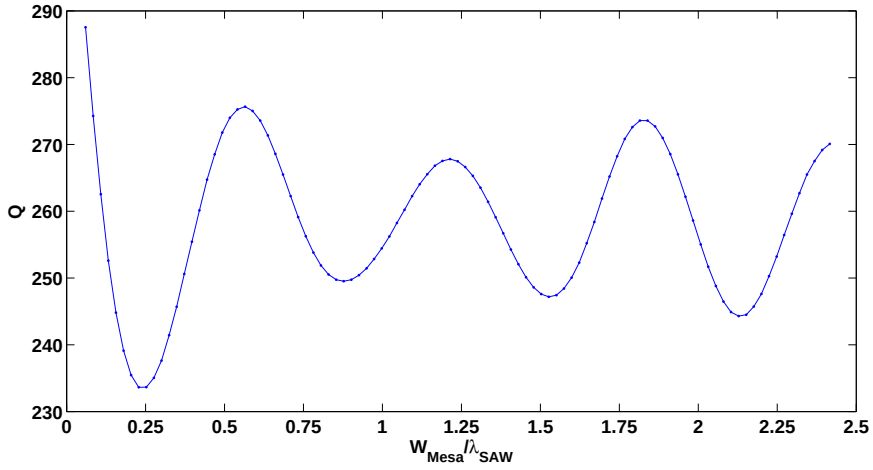

Figure 5.12: Variation of Q as a function of mesa width for a disc oscillator of resonant frequency 1.13 GHz in the second radial mode.The mesa radius is kept constant at $1.25 \times \lambda_{\mathrm{SAW}}$.

Variation of Q with mesa width

The effect of changing mesa width on Q of the system is shown in Figure 5.12. Quality factor of the device again varies periodically with the changing mesa width, the period being the wavelength of the SAW waves.

5.3.2 Source of Error

Some source of errors that might result in a difference between the experiments and simulations are following.

- The material used in the simulations was assumed to be isotropic and although top layer of polysilicon and the intermediate layer of SiO_2 are close to isotropic, the silicon substrate is not isotropic. This might result in some of the error as most of the energy in SAW at these frequencies of motion is concentrated in the silicon for the oscillation frequencies considered here.

- Ideally the mesas should be in the shape of slowness diagram of substrate. They are assumed circular for the FEA and are polygonal for the structures used in experiments. This could also explain some discrepancy between the model and the experiments.

- The top polysilicon layer is under a compressive pre-stress. This causes the buckling in the dome, however this doesn't release entire stress in the polysilicon layer. Prestress was not considered in the simulations and could have resulted in errors.

- Material properties for the in situ deposited, top polysilicon layer were not known accurately. In addition the height of the dome wasn't known accurately. Hence the parameters were optimized to give the best fit for the frequency distribution seen in the experiment. The optimization gave reasonable values for the parameters, however this might produce some error in the absolute magnitude of Q.

Chapter 6

Conclusion

Modeling of the frequency tunability/ entrainment was demonstrated for optically driven disc and buckled dome shaped shell resonators using a parametrically excited coupled thermomechanical model. The model not only captures the complex entrainment behavior of these structures but also predicts the behavior of MEMS for certain parmeter variations. A better understanding of the system otherwise unavailable via numerical integration, such as various bifurcations involved in the entrainment, were revealed by performing a perturbation analysis on this model. Perturbation also helped in determining the importance of various model parameters to accurately describe entrainment. Entrainment was also demonstrated in a combination of certain other canonical systems, which individually captured the disc oscillator behavior for certain specific cases. This not only provides a simpler model for the entrainment but also helps studying the bifurcations in parameter space.

Next a study was performed on the loss mechanism through the anchor into the substrate for the dome/disk resonator. Several modeling techniques to capture the losses were discussed. A finite element framework to calculate anchor loss using the commercial FEA package ABAQUS was developed. Mechanical Q-factors corresponding to the loss to the substrate were calculated. Design improvements were considered to minimize losses associated with the substrate coupling. Since most of the loss in the substrate is associated with the propagation of surface acoustic waves (SAW) a mesa structure was conceived to partially reflect this energy. A mesa is a trench surrounding the dome resonator which acts as a discontinuity in

the propagating medium of the wave. A parametric design analysis was performed on the mesa to determine the dimensions for highest improvement in Q. These results were then verified experimentally on dome shaped resonators where up to four times improvement in Q was obtained. A theoretical analysis based on a delayed feedback system also verified the above results. The reflected wave energy in this case corresponded to the feedback signal.

Entrainment behavior captured by the modeling techniques used above lays the groundwork for future work. The one DOF model developed for the disk resonator could be used to study complex systems such as entrainment in a network of disk/dome oscillators. The perturbation methods used here could also form the basis for analysis of these and other complex systems. Good agreement of entrainment results also points towards a correct understanding of the physics of the problem, hence the models could be used for design purposes.

The modeling techniques used to determine substrate losses can be extended to other geometries and could include effects already available in ABAQUS such as pretension. There are very few methods available to decrease the losses associated with the anchor coupling. Hence mesa structures hold promise for direct implementation to commercial MEMS. This idea can easily be extended to other geometries such as bar resonators, cantilevered beams etc. and is compatible with other existing designs for anchor loss reduction. Since the mesa structure leads to a feedback mechanism, an array of these oscillators coupled together by SAW or electrically would also result in Q improvement. Parametric analysis also shows that the improvement in Q achieved with mesa is an increasing function of the resonator frequency, hence the mesa structure would become even more useful with higher frequency resonators.

APPENDIX A

A.1 Two variable Expansion in the Disc Resonator

Two variable expansion perturbation method [41] applied to the governing eqs.(2.1) and (2.3) involves replacing time t by two time scales, stretched time $\xi = \omega t$ and slow time $\eta = \epsilon t$. Here ω is taken as the forcing frequency, that is, either $\omega = \omega_{\text{piezo}}$ or $\omega = \omega_{\text{laser}}$, depending upon which type of forcing we are considering. (Recall that examples in which both types of forcing are applied are not considered.) To make the following analysis concrete, laser modulation is omitted by taking $\varphi = 0$ in eq.(2.3), and choosing $\xi = \omega_{\text{piezo}} t$.

Next, the displacement z and temperature T are expanded in a series of ϵ:

$$z = Z_0(\xi, \eta) + \epsilon Z_1(\xi, \eta) + O(\epsilon^2) \tag{A.1}$$

$$T = T_0(\xi, \eta) + \epsilon T_1(\xi, \eta) + O(\epsilon^2) \tag{A.2}$$

The forcing frequency $\omega = \omega_{\text{piezo}}$ is detuned off of the natural frequency of the oscillator, which has been scaled to 1 in eq.(2.1):

$$\omega = 1 + \epsilon k_1 + O(\epsilon^2) \tag{A.3}$$

The equation parameters are scaled so that when ϵ=0 eq.(2.1) becomes a simple harmonic oscillator:

$$Q = \frac{Q'}{\epsilon},\ C = C'\epsilon,\ D = D'\epsilon,\ \beta = \beta'\epsilon,\ M = M'\epsilon \tag{A.4}$$

In what follows we make these substitutions in eqs.(2.1) and (2.3), and then drop the primes for convenience.

Making the substitutions (A.1)-(A.4) in eqs.(2.1) and (2.2) and collecting terms in ϵ gives a sequence of differential equations on Z_i and T_i, the first few of which

are:

$$\frac{\partial^2 Z_0}{\partial \xi^2} + Z_0 = 0 \tag{A.5}$$

$$\frac{\partial T_0}{\partial \xi} - BT_0 = AP \tag{A.6}$$

$$\frac{\partial^2 Z_1}{\partial \xi^2} + Z_1 = M \sin\xi - 2k_1 \frac{\partial^2 Z_0}{\partial \xi^2} - 2\frac{\partial^2 Z_0}{\partial \xi \partial \eta} - \frac{1}{Q}\frac{\partial Z_0}{\partial \xi} - CT_0 Z_0 + DT_0 - \beta Z_0^3 \tag{A.7}$$

The general solution of eq.(A.5) is of the form

$$Z_0(\xi, \eta) = X(\eta)\cos\xi + Y(\eta)\sin\xi \tag{A.8}$$

where $X(\eta)$ and $Y(\eta)$ are slowly varying coefficients.

In order to obtain a closed form solution to eq.(A.6), the $\sin^2 2\pi(Z_0 - z_0)$ term in P (see eq.(2.3)) is approximated by the following truncated Taylor expansion, valid for small values of $(Z_0 - z_0)$:

$$\sin^2 2\pi(Z_0 - z_0) \approx 4\pi^2(Z_0 - z_0)^2 + \frac{16\pi^4}{3}(Z_0 - z_0)^4 \tag{A.9}$$

After substituting eqs.(A.8),(A.9) and (2.3)) into eq.(A.6), we used the computer algebra software MACSYMA to solve for the steady state solution T_0. This gives a very large expression which we omit here for brevity. The expression for T_0 so obtained is then substituted, along with eq.(A.8), into eq.(A.7). Then after trigonometric simplification, we proceed with the removal of the secular terms, these being the coefficients of $\sin\xi$ and $\cos\xi$. The result is a pair of slow flow equations which govern the evolution of the slowly varying coefficients $X(\eta)$ and $Y(\eta)$. Since these equations are very long if written out with all the parameters in unevaluated form, we present instead a version of the slow flow which uses the numerical values of the coefficients listed in eqs.(2.4) and $P_{\text{laser}} = 650\mu W$:

$$\begin{aligned}\dot{X} &= -M + a_{1,0}\,X + a_{0,1}\,Y \\ &\quad + a_{3,0}\,X^3 + a_{2,1}\,Y\,X^2 + a_{1,2}\,Y^2\,X + a_{0,3}\,Y^3 \\ &\quad + a_{5,0}\,X^5 + a_{4,1}\,Y\,X^4 + a_{3,2}\,Y^2\,X^3 + a_{2,3}\,Y^3\,X^2 \\ &\quad + a_{1,4}\,Y^4\,X + a_{0,5}\,Y^5 \end{aligned} \tag{A.10}$$

$$\begin{aligned}\dot{Y} &= b_{1,0}\,X + b_{0,1}\,Y \\ &\quad + b_{3,0}\,X^3 + b_{2,1}\,Y\,X^2 + b_{1,2}\,Y^2\,X + b_{0,3}\,Y^3 \\ &\quad + b_{5,0}\,X^5 + b_{4,1}\,Y\,X^4 + b_{3,2}\,Y^2\,X^3 + b_{2,3}\,Y^3\,X^2 \\ &\quad + b_{1,4}\,Y^4\,X + b_{0,5}\,Y^5 \end{aligned} \tag{A.11}$$

where the numerical value of the coefficients $a_{i,j}$ and $b_{i,j}$ is given in A.2.

A.2 Parameters in the Slow Flow of Disc Resonator

The values of the coefficients in eqs.(2.5) and (2.6) are given below:

$a_{1,0} = -0.0004296$

$a_{0,1} = -0.00044719 - k_1$

$a_{3,0} = 0.0000967963$

$a_{2,1} = 1.51401$

$a_{1,2} = 0.0000967963$

$a_{0,3} = 1.51401$

$a_{5,0} = -0.21743$

$a_{4,1} = -0.21743$

$a_{3,2} = -0.06435$

$a_{2,3} = -0.43487$

$a_{1,4} = -0.03218$

$a_{0,5} = -0.21743$

$b_{1,0} = -0.00044719 + k_1$

$b_{0,1} = -0.00004296$

$b_{3,0} = -1.51401$

$b_{2,1} = .0000967963$

$b_{1,2} = -1.51401$

$b_{0,3} = 0.0000967963$

$b_{5,0} = 0.21743$

$b_{4,1} = -0.03218$

$b_{3,2} = 0.43487$

$b_{2,3} = -0.06435$

$b_{1,4} = 0.21743$

$b_{0,5} = -0.03218$

BIBLIOGRAPHY

[1] M. Pandey, K. Aubin, M. Zalalutdinov, A.T. Zehnder, and R.H. Rand. Analysis of frequency locking in optically driven MEMS resonators. *IEEE Journal of Microelectromechanical Systems*, 15 No 6:1546–1554, Dec. 2006.

[2] M. Zalalutdinov, K.L. Aubin, M. Pandey, A.T. Zehnder, R.H. Rand, H.G. Craighead, and J.M. Parpia. Frequency entrainment for micromechanical oscillator. *Applied Physics Letters*, 83:3281–3283, 2003.

[3] K. Aubin, M.Zalalutdinov, T. Alan, R. Reichenbach, R.H. Rand, A.T. Zehnder, J. Parpia, and H. Craighead. Limit cycle oscillations in CW laser driven NEMS. *IEEE/ASME Journal of Micromechanical Systems*, 13:1018–1026, 2004.

[4] Viktorov I.A. Effect of surface defects on propogation of Rayleigh waves. *Soviet Physics. Doklady*, 304-306, 1958.

[5] C. T.-C. Nguyen and R. T. Howe. An integrated CMOS micromechanical resonator high-Q oscillator. *IEEE Journal of Solid-State Circuits*, 34:440445, 1999.

[6] Hornbeck L.J. Digital light processing and MEMS: an overview. In *Advanced Applications of Lasers in Materials Processing*, pages 7–8, 1996.

[7] Ohara K. and Kunzman A. Video processing technique for multimedia HDTV with digital micro-mirror array. In *IEEE Transactions on Consumer Electronics*, volume 45, 1999.

[8] Hammond J.and McNeil A.and August R.and Koury D. Inertial transducer design for manufacturability and performance at Motorola. In *IEEE 12th International Conference on TRANSDUCERS, Solid-State Sensors, Actuators and Microsystems*, volume 1, pages 8–12, 2003.

[9] S. W. Schlosser. *Using MEMS-based storage devices in computer systems.* Ph.D. Thesis Carnegie Mellon University, 2004.

[10] E. H. Callaway. *Wireless Sensor Networks: Architectures and Protocols.* Auerbach Publications, NY, 2004.

[11] A.-C. Wong Nguyen C.T.-C and H. Ding. RF MEMS for wireless Applications. *IEEE Intl. Solid-State Circuits Conference*, 448:78, 1999.

[12] K. L. Aubin, M. Zalautdinov, R. B. Reichenbach, B. Houston, A. T. Zehnder, J. M. Parpia, and H. G. Craighead. Laser annealing for high-Q MEMS resonators. *Proceedings of SPIE*, 5116:531–535, 2003.

[13] M. Reinstadtler, U. Rabe, V. Scherer, U.Hartmann, A.Goldade, B.Bhushan, and W. Arnold. On the nanoscale measurement of friction using atomic-force microscope cantilever torsional resonances. *Applied Physics Letters*, 82:2604–2606, 2003.

[14] J. A. Sidles, J. L. Garbini, K. J. Bruland, D. Rugar, O. Zuger, S. Hoen, and C. S. Yannoni. Magnetic resonance force microscopy. *Review of Modern Physics*, 67:249, 1995.

[15] D. Sarid. *Scanning Force Microscopy With Applications to Electric, Magnetic and Atomic Forces*. Oxford University Press, New York, 1994.

[16] Nguyen C.T.-C. RF MEMS for wireless Applications. *Device Research Confrence*, 60th DRC Confrence digest:9–12, 2002.

[17] S. Lee, M. U. Demirci, and C. T. C. Nguyen. A 10-MHz micromechanical resonator Pierce reference oscillator for communications. In *Digest of Technical Papers, the 11th International Conference on Solid-State Sensors and Actuators (Transducers01)*, pages 1094–1097, June 2001.

[18] A.-C. Wong and C.T.-C. Nguyen. Micromechanical mixer-filters (mixlers). *IEEE Journal of MicroElectromechanical Systems*, 13:100112, Feb. 2004.

[19] R. C. Rennick. An equivalent circuit approach to the design and analysis of monolithic crystal filters. *IEEE Journal of Solid-State Circuits*, SU-20:347354, Oct. 1973.

[20] H. Khorramabadi and P.R. Gray. High-frequency CMOS continuous time filters. *IEEE Journal of Solid-State Circuits*, SC-19:939948, 1984.

[21] M. Zalalutdinov, K. Aubin, C. Michael, R. Reichenbach, T. Alan, A.T. Zehnder, B. Houston, J. Parpia, and H. Craighead. Shell-type micromechanical oscillator. In *Microtechnolgies for the New Millenium*. SPIE, 2003.

[22] M. Zalalutdinov, A. T. Zehnder, A. Olkhovets, S. Turner, L. Sekaric, B. Ilic, D. Czaplewski, J. M. Parpia, and H. G. Craighead. Autoparametric optical drive for micromechanical oscillators. *Applied Physics Letters*, 79:695–697, 2001.

[23] K. L. Turner, S. A. Miller, P. G. Hartwell, N. C. MacDonald, S. H. Strogatz, and S.G. Adams. Five parametric resonances in a microelectromechanical system. *Nature*, 396:149–152, 1998.

[24] W. Zhang, R. Baskaran, and K. L. Turner. Effect of cubic nonlinearity on autoparametrically amplified resonant MEMS mass sensor. *Sensors and Actuators A*, 102:139–150, 2002.

[25] D. Rugar and P. Grütter. Mechanical parametric amplification and thermomechanical noise squeezing. *Phsical Review Letters*, 67:699–702, 1991.

[26] D. W. Carr, S. Evoy, L. Sekaric, H. G. Craighead, and J. M. Parpia. Parametric amplification in a torsional microresonator. *Applied Physics Letters*, 77:1545–1547, 2000.

[27] M.-F. Yu, G. J. Wagner, R.S. Ruoff, and M. J. Dyer. Realization of parametric resonance in a nanowire mechanical system with nanomanipulation inside a scanning electron microscope. *Physical Review B*, 66:1–4, 2002.

[28] L. Sekaric, M. Zalalutdinov, R. B. Bhiladvala, A. T. Zehnder, J.M. Parpia, and H. G. Craighead. Operation of nanmechanical resonant structures in air. *Applied Physics Letters*, 81:2641–2643, 2002.

[29] M. Zalalutdinov, A. Olkhovets, A. T. Zehnder, B. Ilic, D. Czaplewski, H. G. Craighead, and J. M. Parpia. Optically pumped parametric amplification for micromechanical oscillators. *Applied Physics Letters*, 78:3142–3144, 2001.

[30] M. Zalalutdinov, K.L. Aubin, M. Pandey, A.T. Zehnder, R.H. Rand, H.G. Craighead, and J.M. Parpia. Frequency entrainment for micromechanical oscillator. *Applied Physics Letters*, 83:3281–3283, 2003.

[31] M. Pandey. *Entrainment in Disc Shaped MEMS oscillator*. M.S. Thesis, Cornell University, 2003.

[32] F. R. Blom, S. Bouwstra, M. Elwenspoek, and J .H. J. Fluitman. Dependence of the quality factor of micromachined silicon beam resonators on pressure and geometry. *J. Vac. Sci. Technol. B*, 10:19–26, 1992.

[33] A. G. Olkhovets. *Nano Electro Mechanical Systems and Their Applications*. Cornell University Ithaca NY 14853, Ph.D. Thesis 2002.

[34] K. Wang, A.-C. Wong, and C.T.-C. Nguyen. VHF free-free beam high-Q micromechanical resonators. *Ultramicroscopy*, 9:347–360, 2000.

[35] J. Wangand, J. E. Butler, T. Feygelson, and C. T.-C. Nguyen. 1.51-GHz. nanocrystalline diamond micromechanical disk resonator with material-mismatched isolating support. In *17th Int. IEEE Micro Electro Mechanical Systems Conf*, pages 641–644, Maastricht, The Netherlands, Jan. 25-29 2004.

[36] J. F. Duffy and Jr. K. P. Wright. Entrainment of the human circadian system by light. *Journal of Biological Rhythms*, 20 No 4:326–338, 2005.

[37] L. M. Pecora and T. L. Carroll. Synchronization in chaotic systems. *Phys. Rev. Lett.*, 64:821824, 1990.

[38] K.Y. Tsang, R.E. Mirillo, S.H. Strogatz, and K. Weisenfeld. Dynamics of globally coupled oscillator array. *Physica D*, 48:102, 1991.

[39] R.E. Mirollo and S.H. Strogatz. Synchronisation of pulse coupled biological oscillators. *SIAM Journal of Applied Mathematics*, 50:1645, 1990.

[40] M.Zalalutdinov, J.Parpia, K.Aubin, H.Craighead, T.Alan, A.Zehnder, and R.Rand. Hopf bifurcation in a disk-shaped nems. *Proceedings of the 2003 ASME Design Engineering Technical Conferences, 19th Biennial Conference on Mechanical Vibrations and Noise, Chicago, IL, Sept. 2-6, 2003, paper no.DETC2003-48516*, 2003.

[41] R.H. Rand. Lecture Notes in Nonlinear Vibrations *(version 45)*. Published on-line by The Internet-First University Press, Ithaca, NY, http://dspace.library.cornell.edu/handle/1813/79, 2004.

[42] A.H. Nayfeh and D.T. Mook. *Nonlinear Oscillations*. Wiley-Interscience, NY, 1979.

[43] E.J. Doedel, R.C.Paffenroth, A.R. Champneys, T.F. Fairgrieve, Y.A. Kuznetsov, B.E. Oldeman, B. Sandsted, and X. Wang. *AUTO 2000: Continuation and Bifurcation Software for Ordinary Differential Equations*. available on line at: http://sourceforge.net/project/showfiles.php?group_id=21781, 2002.

[44] M. Pandey, R.H. Rand, and A.T. Zehnder. Perturbation analysis of entrainment in a micromechanical limit cycle oscillator. *Communications in Nonlinear Sciences and Numerical Simulation*, accepted December 2005.

[45] Z. Haoa, A. Erbil, and F. Ayazi. An analytical model for support loss in micromachined beam resonators with in-plane flexural vibrations. *Sensors and Actuators*, 109:156164, 2003.

[46] Y. H. Park and K. C. Park. High-fidelity modeling of MEMS resonators. part I. anchor loss mechanisms through substrate. *IEEE Journal of MicroElectromechanical Systems*, 13:238–247, April 2004.

[47] Y. H. Park and K. C. Park. High-fidelity modeling of MEMS resonators. part II. anchor loss mechanisms through substrate. *IEEE Journal of MicroElectromechanical Systems*, 13:248–257, April 2004.

[48] F.H. Lei, J.-L. Nicolas, and M.Troyon. Perfectly matched layers for time-harmonic elastodynamics of unbounded domains:theory and finite-element implementation. *Computer Methods in Applied Mechanics and Engineering*, 192:1337–1375, 2003.

[49] D.S. Bindel, E. Quevy, T. Koyama, S. Govindjee, J.W. Demmel, and R.T. Howe. Anchor loss simulation in resonators. In *Proceedings of MEMS 2005*, page 133136, Miami, FL, February 2005.

[50] *Abaqus Manual v 6.4*. Abaqus Inc., 2004.

[51] S. D. Senturia. *Microsystem Design.* Kluwer Academic Publishers, Norwell, MA, 2001.

[52] D. Bindel. available online at http://www.cs.berkeley.edu/ dbindel /hiqlab/.

[53] G.F. Miller and H. Pursey. On the partition of energy between elastic waves in a semi-infinite solid. *Proceedings of the Royal Society of London*, 233, 1955.

[54] S.Gao, L.F.Chi, S.Lenert, B.Anczykowski, C.Neimeyer, M.Adler, and H.Fuchs. High-quality mapping of DNA-protien complexes by dynamic scanning force microscopy. *ChemPhysChem*, 6:384, 2001.

[55] T.Sulchek, R.Hsieh, J.D.Adams, G.G.Yaralioglu, S.C.Minne, C.F.Quate, J.P.Cleveland, A. Atlar, and D.M.Adderton. High-speed tapping mode imaging with active Q control for atomic force microscopy. *Applied Physics Letters*, 76:1473, 2000.

[56] J.Tamayo, A.D.L.Humphris, A.M.Malloy, and M.J.Miles. Chemical sensors and biosensors in liquid environment based on microcantilevers with amplified quality factor. *Ultramicroscopy*, 86:167, 2001.

[57] W.J Hall and N.M. Newmark. *Vibrations of Soils and Foundations.* T. Prentice Hall Inc.,Englewood Cliffs, New Jersey, 1970.

[58] S. E. Kattis, D. Polyzos, and D. E. Beskos. Vibration isolation by a row of piles using a 3-D frequency domain BEM. *International Journal for Numerical Methods in Engineering*, 46:713–728, 1999.

[59] R. B. Reichenbach, M. Zalalutdinov, K. L. Aubin, R. Rand, B. Houston, J. M. Parpia, , and H. G. Craighead. Third-order intermodulation in a micromechanical thermal mixer. *J. Microelectromech. Syst.*, 14:1244–1252, Dec. 2005.

[60] M. Zalalutdinov, K. L. Aubin, R. B. Reichenbach, A. T. Zehnder, B. Houston, J. M. Parpia, and H. G. Craighead. Shell-type micromechanical actuator and resonator. *Applied Physical Letters*, 83:3815–3817, 2003.

[61] B. Ilic, S. Krylov, K. Aubin, R. B. Reichenbach, and H. G. Craighead. Optical excitation of nanoelectromechanical oscillators. *Appl. Phys. Lett.*, 86, 2005.

[62] M. Zalalutdinov, K. L. Aubin, and R. B. Reichenbach. Shell-type micromechanical oscillator. In *Microtechnologies for the New Millennium, SPIE*, 2003.

[63] C. Zener. *Elasticity and Inelasticity of Metals.* The University of Chicago Press,Chicago, 1948.

[64] B.H. Houston, D. M. Photiadis, M.H. Marcus, J.A. Bucaro, and Xiao Liu. Thermoelastic loss in microscale oscillators. *Applied Physics Letters*, 80:1300–1302, 2002.